Mon. Not. R. Astron. Soc. **000**, 000–000 (0000) Printed 4 February 2010 (MN LATEX style file v2.2)

Extragalactic gamma-ray background radiation from dark matter annihilation

Jesús Zavala[1,2⋆], Volker Springel[1] and Michael Boylan-Kolchin[1]

[1] *Max-Planck-Institut für Astrophysik, Karl-Schwarzschild-Straße 1, 85740 Garching bei München, Germany*
[2] *MPA/SHAO Joint Center for Astrophysical Cosmology at Shanghai Astronomical Observatory, Nandan Road 80, Shanghai 200030, China*

4 February 2010

ABSTRACT

If dark matter is composed of neutralinos, one of the most exciting prospects for its detection lies in observations of the gamma-ray radiation created in pair annihilations between neutralinos, a process that may contribute significantly to the extragalactic gamma-ray background (EGB) radiation. We here use the high-resolution Millennium-II simulation of cosmic structure formation to produce the first full-sky maps of the expected radiation coming from extragalactic dark matter structures. Our map making procedure takes into account the total gamma-ray luminosity from all haloes and their subhaloes, and includes corrections for unresolved components of the emission as well as an extrapolation to the damping scale limit of neutralinos. Our analysis also includes a proper normalization of the signal according to a specific supersymmetric model based on minimal supergravity. The new simulated maps allow a study of the angular power spectrum of the gamma-ray background from dark matter annihilation, which has distinctive features associated with the nature of the annihilation process and may be detectable in forthcoming observations by the recently launched FERMI satellite. Our results are in broad agreement with analytic models for the gamma-ray background, but they also include higher-order correlations not readily accessible in analytic calculations and, in addition, provide detailed spectral information for each pixel. In particular, we find that difference maps at different energies can reveal cosmic large-scale structure at low and intermediate redshifts. If the intrinsic emission spectrum is characterized by an emission peak, cosmological tomography with gamma ray annihilation radiation is in principle possible.

Key words: cosmology: dark matter – methods: numerical

1 INTRODUCTION

The nature of dark matter in the Universe is one of the most fascinating and important mysteries of astrophysics today. Based on the evidence gathered during the last decades, we know that a suitable particle physics candidate has to be neutral and stable (or with a lifetime comparable to the age of the Universe) to be the major component of dark matter, and that its interactions with ordinary matter have to be very weak in order to be consistent with constraints from cosmic structure formation.

Among the different theories that propose a solution to the dark matter problem, supersymmetric (SUSY) extensions of the standard particle physics model with R-parity conservation are particularly attractive (see for example Martin 1998, for a pedagogical introduction to SUSY). They generically predict the existence of a lightest supersymmetric particle (LSP), which appears as a plausible dark matter candidate. Among the possible LSPs resulting from SUSY theories, two are strongly motivated and have been studied in detail: the gravitino, which is the spin-3/2 superpartner of the graviton, and the lightest neutralino, the spin-1/2 Majorana fermion that appears in the Minimal Supersymmetric Standard Model (MSSM) as the lightest mass eigenstate of a mixture of the superpartners of the neutral gauge bosons (the fermions $\tilde{B}^0$ and $\tilde{W}^0$) and the neutral SUSY Higgs ($\tilde{H}_u^0$ and $\tilde{H}_d^0$). Although gravitinos are interesting viable candidates to be the major component of dark matter (see for instance Feng (2005); Steffen (2006) for recent reviews), they can be classified as *extremely* weakly interacting particles (Steffen 2007) and are therefore very hard to detect experimentally. On the other hand, the character of neutralinos as Majorana fermions (they are their own antiparticle) and their somewhat stronger interactions as just weakly interact-

⋆ e-mail: jesus@mpa-garching.mpg.de

ing massive particles (WIMPs) make them more promising candidates for detection, possibly in the near future.

Being WIMPs with expected masses of the order of 100 GeV, neutralinos have all the properties required to be the cold dark matter (CDM) in the prevailing ΛCDM cosmogony, which is at present the most successful model of structure formation (e.g. Komatsu et al. 2009; Springel et al. 2006). Significant efforts are therefore undertaken to find experimental proof for the existence of neutralinos. These experiments are usually classified as direct and indirect searches (for recent reviews on direct and indirect dark matter searches in the Galaxy see Bertone 2007; Hooper 2007; Spooner 2007; de Boer 2008).

Direct dark matter search experiments look for the recoil of ordinary matter by scattering of WIMPs in laboratories on Earth. Some of the experiments that have been looking for signals are: CDMS (Akerib et al. 2004), XENON (Angle et al. 2008), ZEPLIN (Alner et al. 2005) and DAMA (Bernabei et al. 2000, 2008). The latter is the only experiment that has reported a positive signal so far, a finding that has not yet been confirmed by another experiment, however.

The interaction rate of neutralinos with ordinary nuclei fundamentally depends on two factors, the flux of neutralinos on Earth and the interaction cross section of neutralinos with a given nuclei. The latter can be computed theoretically within the context of the SUSY model, but the former depends strongly on the phase space distribution of dark matter at the Solar circle, which needs to be predicted by cosmological models of structure formation. In standard analysis, a constant dark matter density and a simple Maxwell-Boltzmann distribution for the particle velocities is often assumed, properly modified to include the motion of the Sun around the Galaxy and that of the Earth around the Sun (Freese et al. 2001). However, it is not at all clear that this simple assumption is justified, because cold dark matter is expected to produce a large number of overlapping cold streams locally, and may leave residual structure in energy space. High-resolution N-body simulations of structure formation combined with an explicit modelling of the local stream density evolution provide one promising new approach to provide a more accurate characterization of the possible signal (Vogelsberger et al. 2008, 2009). Other dynamical local Solar System effects may also be important (Lundberg & Edsjö 2004).

Indirect dark matter searches look for the products of WIMP annihilations generated in cosmic structures. Such possible annihilation products include, for example, positrons (Baltz & Edsjö 1999), neutrinos (Berezinsky et al. 1996) and gamma-ray photons. Interestingly, the satellite PAMELA has recently reported an anomalously high positron abundance in cosmic rays at high energies (Adriani et al. 2009). Although this signal could be explained by a number of astrophysical sources, dark matter annihilations offer a particularly attractive explanation under certain scenarios (Bergström et al. 2008), and this possibility has created a flurry of activity in the field. In a related experiment, the FERMI satellite has measured an excess in the total flux of electrons and positrons in cosmic rays (Abdo et al. 2009), which, although is smaller than those reported by the balloon experiments ATIC and PPB-BETS (Chang et al. 2008; Torii et al. 2008) is nevertheless significant.

Within our Galaxy, the annihilation signal is expected to be particularly strong in the high density regions around the galactic centre (Bertone & Merritt 2005; Jacholkowska et al. 2006). However, since other astrophysical sources contribute prominently to the gamma-ray flux there, it may be difficult to disentangle a possible neutralino annihilation signal from the rest of "ordinary" sources. A more promising approach may lie in an analysis of the gamma-ray radiation produced in the smooth Milky Way halo as a whole (Stoehr et al. 2003; Fornengo et al. 2004; de Boer et al. 2004; Springel et al. 2008). Particular attention has also been given to substructures within the MW halo (e.g. Siegal-Gaskins 2008; Ando 2009), which have been suggested to dominate the annihilation signal observed at Earth (Berezinsky et al. 2003), even though they have recently been shown to be more difficult to detect compared with the signal from the galactic centre (Springel et al. 2008). Searches in other nearby galaxies have also been considered, such as Andromeda (Falvard et al. 2004; Lavalle et al. 2006) and other galaxies in the Local Group (Wood et al. 2008). Clusters of galaxies may also be interesting targets for searches (Jeltema et al. 2009) due to their large content of dark matter, even though a variety of other possible sources of high energy gamma-rays in clusters, such as cosmic rays generated in structure formation shocks, active galactic nuclei and supernovae, can lead to confusion and may make it challenging to cleanly separate the dark matter signal from the confusing sources.

On still larger scales, we expect that traces of dark matter annihilation should be present in the extragalactic gamma-ray background (EGB) radiation, which contains gamma-rays coming from all possible cosmic sources. In the present work, we will focus on these *extragalactic* gamma-ray photons. The EGB has been measured by different gamma-ray satellites, in particular in the energy range between 1 MeV and 30 GeV by COMPTEL and EGRET (Strong et al. 2004). In the near future, our understanding of the EGB will greatly improve by the Large Area Telescope aboard the recently launched FERMI satellite (formerly known as GLAST, Atwood et al. 2009), which covers an energy range between 20 MeV and 300 GeV and features a greatly improved sensitivity compared with its predecessor EGRET. Several sources of different astrophysical origin are known to contribute significantly to the EGB, including blazars (Ando et al. 2007a; Kneiske & Mannheim 2008), type Ia supernovae (Strigari et al. 2005), cosmic rays accelerated at cosmological structure formation shocks (Miniati 2002; Miniati et al. 2007; Jubelgas et al. 2008), among others (see Dermer 2007; Kneiske 2008, for recent reviews). Of course, dark matter annihilation also contributes to the EGB, and it is in this component that we focus on in this work.

Using standard analytic approaches to describe cosmic structure formation, like halo mass functions and clustering amplitude as a function of redshift, it is possible to make predictions for the relative gamma-ray flux coming from haloes and their subhaloes as a function of mass and redshift (Ullio et al. 2002; Taylor & Silk 2003) and to use this information to estimate the contribution of dark matter annihilation to the EGB. Both, the isotropic and anisotropic components of this radiation have been predicted in this way in previous works (Elsässer & Mannheim

2005; Ando & Komatsu 2006; Cuoco et al. 2007, 2008; de Boer et al. 2007; Fornasa et al. 2009). In particular, Ando & Komatsu (2006) first pointed out that the density squared dependence of dark matter annihilation should leave a specific signature in the angular power spectrum of the EGB. We also note that Siegal-Gaskins & Pavlidou (2009) have shown that the energy dependence of the angular power spectrum of the total diffuse gamma-ray emission can be used to disentangle different source populations, including that associated with dark matter annihilation.

However, it is not clear how accurately these analytic approaches capture the non-linear structures resolved in the newest generation of high-resolution cosmological simulations. Also, the previous analysis have so far been restricted to statistical statements about the power spectrum of the EGB, or its mean flux. For a full characterization of the signal, it would be useful to have accurate realizations of maps of the expected gamma-ray emission over the whole sky. Such maps contain in principle the full information that can be harvested, and allow, for example, correlation studies with foreground large-scale structure in terms of galaxies or dark matter.

In the present paper, we therefore focus on techniques to predict the extragalactic gamma-ray background directly from cosmological N-body simulations. To this end, we use the Millennium-II simulation. With 10^{10} particles in a homogeneously sampled volume of $(100\,h^{-1}\mathrm{Mpc})^3$, it is one of the best resolved structure formation simulations to date. We use a ray-tracing technique to accumulate the signal from all haloes and subhaloes over the past light-cone of a fiducial observer, positioned at a plausible location of the Milky Way in the simulation box. Through careful accounting for unresolved structure, we can extrapolate our signal to the damping scale limit and obtain the first realization of realistic full sky maps of the expected gamma-ray radiation from dark matter annihilation. The maps can be used both to check earlier analytic estimates, and to develop new strategies for identification and exploitation of the annihilation component in the EGB. For example, we show that difference maps at different energies could be used to uncover nearby cosmic large-scale structure, which could be correlated with other probes of large-scale structure to more unambiguously identify the origin of this background component.

This paper is organized as follows. In Section 2, we briefly review the analytic formulae associated with the contribution to the EGB from dark matter annihilation. In Section 3, we describe the SUSY model chosen for our analysis. We then present the N-body simulation used, and the effect of dark matter clustering in the annihilation's gamma ray flux in Section 4. In Section 5 we describe our method to generate simulated sky maps of the EGB radiation from dark matter annihilation, and we analyse the energy and angular power spectra of the signal. We give a summary and our conclusions in Section 6.

2 DARK MATTER ANNIHILATION RATES AND THE EGB

If dark matter is made of particles that can annihilate with each other, then the number of annihilations per unit time in a given volume V is given by (e.g. Gondolo & Gelmini 1991):

$$n = \frac{\langle\sigma v\rangle}{2m_\chi^2}\int_V \rho_\chi^2(\boldsymbol{x})\,\mathrm{d}^3x, \tag{1}$$

where m_χ and ρ_χ are the mass and density of the dark matter species, and $\langle\sigma v\rangle$ is the thermally averaged product of the annihilation cross section and the Møller velocity.

Since the particle physics details related to the intrinsic nature of dark matter are encoded in the term outside the integral in Eq. (1), it is convenient to remove this dependence in analyzing the effect of dark matter clustering on the annihilation rate. For this purpose, it is customary to introduce the ratio of gamma ray emission coming from a given halo of volume V to the average emission of a homogeneous distribution of the same amount of dark matter within this volume:

$$f_h(V) = \frac{1}{\bar\rho_h^2 V}\int_V \rho_\chi^2(\boldsymbol{x})\,\mathrm{d}^3x \tag{2}$$

where $\bar\rho_h$ is the average density of dark matter particles inside V.

For instance if the region of interest is a dark matter halo, then Eq. (2) can be solved analytically by assuming a specific density distribution. In particular, for the spherically symmetric NFW profile (Navarro et al. 1997), $f_h(V)$ is given by (Taylor & Silk 2003):

$$f_h(c_\Delta) = \frac{c_\Delta^3\left[1-1/(1+c_\Delta^3)\right]}{9\left[\ln(1+c_\Delta)-c_\Delta/(1+c_\Delta)\right]^2}, \tag{3}$$

where $c_\Delta = r_\Delta/r_s$ is the concentration parameter, r_s is the scale radius of the NFW profile, and r_Δ is the limiting radius of the halo, connected to its enclosed mass M_Δ through:

$$M_\Delta = \frac{4}{3}\pi\bar\rho_h r_\Delta^3 = \frac{4}{3}\pi\Delta\rho_{\mathrm{crit}} r_\Delta^3, \tag{4}$$

where Δ is the overdensity parameter. Different values for Δ are used in the literature, with the two main choices being $\Delta = 200$ (Navarro et al. 1997), and $\Delta \sim 178\Omega_m^{0.45}$ for a ΛCDM model with $\Omega_m + \Omega_\Lambda = 1$ (Eke et al. 2001).

For spherically symmetric haloes, the integral in Eq. (2) can also be written as the scaling law (Springel et al. 2008) $L'_h \propto V_{\mathrm{max}}^4/r_{\mathrm{half}}$, where V_{max} is the maximum rotational velocity of the halo and r_{half} is the radius containing half of the gamma-ray flux. For a NFW halo, the latter formula reduces to

$$L'_h = \int \rho_{\mathrm{NFW}}^2(r)\,\mathrm{d}V = \frac{1.23\,V_{\mathrm{max}}^4}{G^2 r_{\mathrm{max}}}, \tag{5}$$

where r_{max} is the radius where the rotation curve reaches its maximum. We will use Eq. (5) for our analysis in this paper. The most recent high-resolution N-body simulations support a slightly revised density profile that becomes gradually shallower towards the centre (Navarro et al. 2009), deviating from the asymptotic power-law cusp of the NFW profile. For this Einasto profile, the coefficient 1.23 in Eq. (5) changes to 1.87, an insignificant difference compared to other uncertainties in the analysis of the dark matter annihilation radiation.

We can extend Eq. (2) to larger volumes containing several haloes of different sizes. If we assume that all dark matter particles in a given cosmic volume V_B belong to virialized

haloes, then the ratio of gamma-ray emission coming from all haloes contained in V_B with masses larger than $M_{\rm min}$ to the emission produced by a smooth homogeneous distribution of dark matter, with average density $\bar{\rho}_B$, filling this volume is given by:

$$f(M > M_{\rm min}) = \frac{1}{\bar{\rho}_B^2 V_B} \int_{M_{\rm min}}^{\infty} {\rm d}N_{V_B}(M) \bar{\rho}_h^2 V(M) f_h(V(M)) \quad (6)$$

where ${\rm d}N_{V_B}(M)$ is the number of haloes in the volume V_B with masses in the range $[M, M+{\rm d}M]$, which can be written as

$${\rm d}N_{V_B}(M) = V_B \frac{{\rm d}n(M)}{{\rm d}M} {\rm d}M = V_B \frac{{\rm d}n(M)}{{\rm dlog}M} {\rm dlog}M, \quad (7)$$

with ${\rm d}n(M)/{\rm dlog}M$ denoting the differential halo mass function. Thus:

$$f(M > M_{\rm min}) = \frac{1}{\bar{\rho}_B^2} \int_{M_{\rm min}}^{\infty} \left(\frac{{\rm d}n(M)}{{\rm dlog}M} \right) \bar{\rho}_h^2 V(M) f_h(V(M)) {\rm dlog}M. \quad (8)$$

In the literature, $f(M > M_{\rm min})$ has been called the "flux multiplier" (Eq. 18 of Taylor & Silk 2003) or the "clumping factor" (Eq. 6 of Ando & Komatsu 2006). The limiting lower mass in Eq. (8) is the minimum mass scale for virialized haloes surviving today, which is roughly given by the free streaming length of dark matter particles: $\sim 10^{-6} M_\odot$ for $m_\chi = 100\,{\rm GeV}$ (Hofmann et al. 2001; Green et al. 2004), see section 4.1 for a discussion on this cutoff mass. Although many of the small scale haloes have suffered from tidal truncation or were disrupted, it is possible that they contribute significantly to the gamma-ray emission produced by dark matter annihilation.

Eqs. (2) and (8) allow us to study the gamma ray flux coming from individual haloes or groups of haloes in a given region of the Universe at a given redshift (both can be applied to any redshift, provided that ρ_χ, $\bar{\rho}_h$ and $\bar{\rho}_B$ are computed at such redshift).

Following Eq. (1), we define the gamma ray emissivity (energy emitted per unit energy range, unit volume and unit time) associated with dark matter annihilation as

$$\epsilon_\gamma = E_\gamma \frac{{\rm d}N_\gamma}{{\rm d}E_\gamma} \frac{\langle \sigma v \rangle}{2} \left[\frac{\rho_\chi}{m_\chi} \right]^2, \quad (9)$$

where ${\rm d}N_\gamma/{\rm d}E_\gamma$ is the total differential photon spectrum summed over all channels of annihilation. Of all the quantities in this equation, only ρ_χ depends on the spatial distribution of dark matter, the rest is related to its intrinsic properties. For the analysis of the latter, since we consider dark matter to be made of neutralinos within a SUSY scenario, we conveniently define the so called SUSY factor[1]:

$$f_{\rm SUSY} = \frac{{\rm d}N_\gamma}{{\rm d}E_\gamma} \frac{\langle \sigma v \rangle}{m_\chi^2}. \quad (10)$$

The signal that we are ultimately interested in is the contribution of neutralino annihilation to the EGB, or more specifically, the spatial distribution of the gamma-ray radiation coming from dark matter annihilation integrated over all redshifts along the line-of-sight for a fiducial observer, located at $z = 0$, for all directions on its two-dimensional full sky. The values we want to calculate for each pixel of such a sky map are that of the specific intensity, the energy of photons received per unit area, time, solid angle and energy range:

$$I_{\gamma,0} = \frac{1}{4\pi} \int \epsilon_{\gamma,0}(E_{\gamma,0}(1+z), z) \frac{{\rm d}r}{(1+z)^4}, \quad (11)$$

where the integral is over the whole line of sight, r is the comoving distance and $E_{\gamma,0}$ is the energy measured by the observer at $z = 0$. Note that $\epsilon_{\gamma,0}$ is evaluated at the blueshifted energy $(1+z)E_{\gamma,0}$ along the line-of-sight to compensate for the cosmological redshifting.

3 DARK MATTER ANNIHILATION AND THE SUSY FACTOR

In the present section we describe the particular SUSY model that we used to compute the gamma-ray emissivity produced by dark matter annihilation. In particular, we provide a closer examination of the SUSY factor given in Eq. (10).

A detailed particle physics model for the nature of the neutralino as dark matter, and its mass and interactions, is needed to compute $f_{\rm SUSY}$. We restrict our analysis to the framework of the minimal supergravity model (mSUGRA, for reviews see Nilles 1984; Nath 2003). The mSUGRA model is popular, among other reasons, due to its relative simplicity, which reduces the large number of parameters in the general MSSM ($\gtrsim 100$) to effectively four free parameters, $m_{1/2}$, m_0, tanβ, A_0 and the choice of sign for μ. The parameters $m_{1/2}$, m_0 and A_0 are the values of the gaugino and scalar masses and the trilinear coupling, all specified at the GUT scale, tanβ is the ratio of the expectation values in the vacuum of the two neutral SUSY Higgs ($\tilde{H}_u^0$ y $\tilde{H}_d^0$), and finally, μ is the Higgsino mass parameter.

The general 5-dimensional parameter space of the mSUGRA model is significantly constrained by various requirements: consistency with radiative electroweak symmetry breaking (EWSB) and experimental constraints on the low energy region, which are given by current lower mass bounds for the lightest SUSY Higgs after EWSB, m_h, as well as concordance between experimental and theoretical predictions for the decay $b \to s\gamma$ and the anomalous magnetic moment of the muon $(g_\mu - 2)/2$. Importantly, it is normally also assumed that the major component of dark matter is the LSP of the theory, then the LSP must be neutral and $\Omega_{\rm LSP} = \Omega_{\rm DM}$, which reduces the allowed regions in the parameter space considerably. For typical mSUGRA scenarios, the LSP that satisfies these conditions is the lightest neutralino. Its relic density Ω_χ needs to be properly calculated by solving the Boltzmann equation, with the parameters of the theory chosen such that the desired dark matter density results.

Observational constraints on the abundance of dark matter, $\Omega_{\rm DM}$, come from various sources, including the cosmic microwave background (CMB), galaxy clusters, supernovae, Lyman-α forest data, and weak gravitational lensing. For the purposes of the analysis in this section, we take the 1σ bound for the amount of dark matter in the Universe

[1] This term has been extensively used previously in the literature, for example in Fornengo et al. (2004), $f_{\rm SUSY}$ is related to the integral quantity $\Phi^{\rm SUSY}$ defined there.

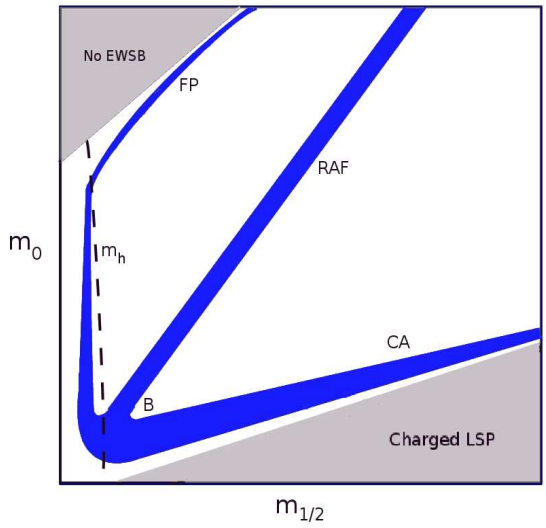

Figure 1. Sketch showing the allowed parameter space of the mSUGRA model when the constraint on the relic density according to Eq. (12) (dark blue region) is imposed. The experimental constraint on the mass of the lightest SUSY Higgs, m_h, is also shown for reference. The grey region in the lower right corner is where the LSP is charged, whereas in the grey region in the upper left corner there is no radiative EWSB. The abbreviated names for various important regions in the parameter space are marked in the figure with capital letters, see text for details.

according to the five year results of WMAP data combined with distance measurements from type Ia supernovae and Baryon Acoustic Oscillations (Komatsu et al. 2009):

$$0.1109 \leqslant \Omega_{\rm DM} h^2 \leqslant 0.1177. \qquad (12)$$

The general picture for the allowed regions in the parameter space of the mSUGRA model resulting from the different constraints can be qualitatively described in the 2-dimensional plane $(m_0 - m_{1/2})$, as shown in Fig. 1. The blue area in the figure represents the allowed region according to Eq. (12) for the observational bounds on the abundance of dark matter.

The different regions in the mSUGRA parameter space that satisfy these constraints have been studied abundantly in the past (e.g. Baer & Balázs 2003; Battaglia et al. 2004; Feng 2005; Bélanger et al. 2005) and have received generic names, marked with capital letters in the figure: (B) bulk region (low values of m_0 and $m_{1/2}$), (FP) focus point region (large values of m_0), (CA) co-annihilation region (low m_0 and $m_\chi \lesssim m_{\tilde{\tau}_1}$, where $\tilde{\tau}_1$ is the lightest slepton) and (RAF) rapid annihilation funnel region (for large values of $\tan\beta$ and a specific condition for m_χ[2]). The regions in grey (light) represent zones where the LSP is charged (lower right corner) and where there is no radiative EWSB solution (upper left corner). The dashed line is shown as a reference for the experimental constraints for m_h.

[2] The relation which should hold is: $2m_\chi \approx m_A$, where A is the CP-odd Higgs boson; see for example Feng (2005) for details.

Our goal in this section is to analyze the supersymmetric factor $f_{\rm SUSY}$ predicted by the mSUGRA model in the different allowed regions depicted in Fig. 1. To do so, we define several "benchmarks points" which fulfill all the experimental constraints discussed above and which can be taken as representative of the different allowed regions in parameter space that we just described. The benchmark points were selected following the analysis of Battaglia et al. (2004) and Gondolo et al. (2004), but slightly modified to be consistent with the cosmological constraint of Eq. (12). We use the numerical code DarkSUSY (Gondolo et al. 2004, 2005) with the interface ISAJET (Baer et al. 2003) to analyse these benchmark points. Table 1 lists the 11 selected benchmark points with their corresponding values for the five mSUGRA parameters, the value of the lightest neutralino's mass, its relic density, and the name of the region they belong to in Fig. 1.

Fig. 2 shows the energy spectrum of $f_{\rm SUSY}$ computed for four of the benchmark points presented in Table 1: A (black dashed line), E (red dotted line), K (green dash-dotted line), and L (blue solid line), which are representatives of the regions CA, FP, RAF and B, respectively. The main features of Fig. 2 are determined by the photon spectrum $\mathrm{d}N_\gamma/\mathrm{d}E_\gamma$ which receives contributions from three mechanisms of photon production (Bringmann et al. 2008): (i) gamma-ray continuum emission following the decay of neutral pions produced during the hadronization of the primary annihilation products at the tree-level; this mechanism is dominant at low and intermediate energies (in Fig. 2 it dominates the spectrum in most of the energy range); (ii) monoenergetic gamma-ray lines for neutralino annihilation in two-body final states containing photons, which is allowed in higher order perturbation theory; the most relevant final states containing these lines are $\chi\chi \to \gamma\gamma$ and $\chi\chi \to Z^0\gamma$, where Z^0 is the neutral Z boson; for non-relativistic neutralinos the energy of each outgoing photons in these processes is $E_\gamma = m_\chi$ and $E_\gamma = m_\chi(1 - m_{Z^0}^2/4m_\chi^2)$, respectively (in Fig. 2 these lines are prominent for benchmark point E (red line) and negligible in the rest of the cases); (iii) when the final products of annihilation are charged, internal bremsstrahlung (IB) needs to be considered, it leads to the emission of an additional photon in the final state; the IB contribution to the spectrum is typically dominant at high energies resulting in a characteristic bump (benchmark points A and L have an important contribution from IB at energies close to m_χ, for the other two points the contribution from IB is negligible). Processes (ii) and (iii) are subdominant relative to process (i), but they display distinctive spectral features intrinsic to the phenomenon of annihilation.

Additionally, the annihilation of neutralinos into electrons and positrons contributes indirectly to the high energy photon spectrum when low energy background photons, such as those in the cosmic microwave background (CMB), are scattered to higher energies via inverse Compton (IC) scattering by these electrons and positrons (Profumo & Jeltema 2009; Belikov & Hooper 2009). In the case of CMB photons, the energy peak of this IC photon emission (E_γ^{IC}) is approximately independent of redshift and is given by: $E_\gamma^{IC} \approx E_\gamma^{CMB}(E_{e^\pm}/m_{e^\pm}c^2)^2$, where E_γ^{CMB} and $E_{e^\pm}$ are the average energies of the CMB photons and $e^\pm$ respectively. For neutralino masses in the 100 GeV range, this energy peak lies in the X-ray regime (~ 10 keV)

Model[a]	A	C	D	E	F	G	H	I	J	K	L
$m_{1/2}$	550	435	520	399	811	396	930	395	750	1300	450
m_0	114	94	113	2977	4307	118.5	242.5	193	299.5	1195	299
tanβ	7	11	10	30	30.4	20	20	35	35	46	47
sign(μ)	+	+	−	+	+	+	+	+	+	−	+
m_χ	226.4	175.1	214.9	154.2	337	160.4	394.2	160.6	315.5	566.1	184.9
$\Omega_\chi h^2$	0.115	0.114	0.116	0.118	0.112	0.113	0.118	0.118	0.114	0.116	0.111
Region[b]	CA	B	CA	FP	FP	B	CA	B	CA	RAF	B

Table 1. Selected benchmark points in the mSUGRA parameter space. For our main analysis, we will focus on point 'L', which predicts an annihilation flux close to the maximum possible for the constrained mSUGRA models.

[a] The letters to represent each point were chosen to follow the notation of Battaglia et al. (2004) and Gondolo et al. (2004)
[b] B for Bulk region, FP for Focus Point region, CA for Co-annihilation region and RAF for Rapid Annihilation Funnel region

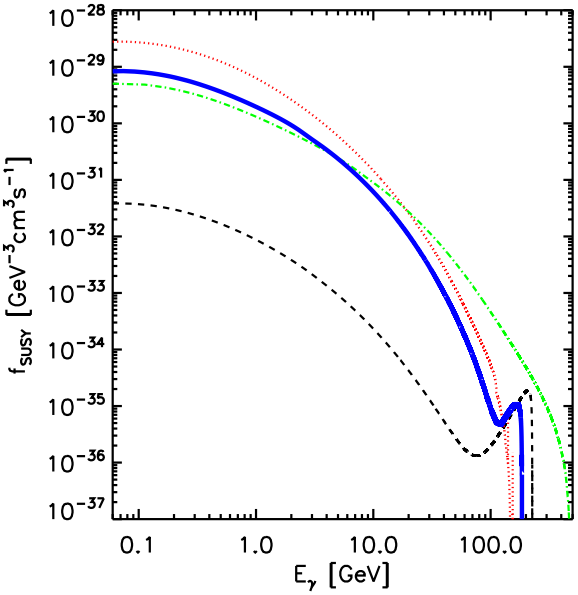

Figure 2. Supersymmetric factor as a function of γ-ray emission energy for a selection of the benchmark points described in Table 1: A, E, K and L, which are shown with black (dashed), red (dotted), green (dash-dotted) and blue (solid) lines, respectively.

(Profumo & Jeltema 2009). Unless the neutralino mass is larger than 1 TeV and with a hard $e^\pm$ spectrum, the contribution of this mechanism is not significant in the energy range relevant to the present study ($\gtrsim 0.1$ GeV). We note that we are currently working on the analysis of the X-ray extragalactic background radiation from dark matter annihilation and we will present our results in a future work.

In Fig. 2, we have shown only 4 of the 11 benchmark points we considered; the rest show very similar features and lie in between these 4 cases. Fig. 2 also indicates that the normalization of the spectrum of $f_{\rm SUSY}$ typically varies by three orders of magnitude among the different regions of the allowed parameter space. Also there appears to be a trend between the different allowed regions in the mSUGRA model: $f_{\rm SUSY}$ has the largest value for benchmark points on the focus point region (FP, red dotted line), followed by the bulk region (B, blue solid line), the rapid annihilation funnel region (RAF, green dash-dotted line), and finally the co-annihilation region (CA, black dashed line). This last feature could be of importance for constraining the allowed mSUGRA parameter space even more: in principle, a precise measurement of the gamma-ray flux coming from dark matter annihilation could discriminate between the characteristic regions FP, B, CA and RAF, considering for example that the difference in $f_{\rm SUSY}$ between the CA and FP regions is around two orders of magnitude. However, such inferences will only become possible if the remaining sources of uncertainty can be reduced to less than two orders of magnitude. This is a demanding goal, given the limited knowledge we have on some of the other astrophysical factors that play an important role in the production of these gamma-rays, as well as the observational difficulties in properly subtracting from an observed gamma-ray signal the contributions from astrophysical sources unrelated to dark matter annihilation. Nevertheless, 'dark matter astronomy' remains an interesting possibility in the light of the results shown in Fig. 2.

In our subsequent analysis, we will now choose one particular benchmark point and adopt its $f_{\rm SUSY}$ value for the rest of our work, keeping in mind the results above. Our chosen benchmark point is the model L (that we highlight with a thick blue solid line in Fig. 2), which gives an upper limit on $f_{\rm SUSY}$ for the benchmark points in the bulk region and is close to the maximum value of $f_{\rm SUSY}$ for all the benchmark points analyzed. The latter is the main reason to choose this particular model because it is desirable that f_{SUSY}, and hence the predicted gamma-ray flux, has a large value among the different theoretical possibilities. This optimistic choice as far as prospects for future detections are concerned then also demarcates the boundary where non-detections can start to constrain the mSUGRA parameter space. But there are other reasons as well. The mass of the neutralino in this model is "safely" larger than the lower mass bounds coming from experimental constraints ($m_\chi > 50$ GeV according to Heister et al. 2004), but low enough to be detectable in the experiments available in the near future. Also, a high value of the parameter tanβ seems to be favored by other theoretical expectations (e.g. Núñez et al. 2008). We note that although benchmark point L does not have prominent gamma-ray lines in its spectrum, it does have an important IB contribution and serves the point of showing the implications of a peak in the annihilation energy spectrum for the EGB.

We note that recent analyses on the cosmic-ray anomalies as measured by PAMELA and FERMI favour higher neutralino masses ($\sim$ 1 TeV) when these anomalies are explained mainly by dark matter annihilation (e.g. Bergström et al. 2009). However, it is important to keep in mind that other astrophysical sources, such as pulsars and supernovae remnants, are expected to have a meaningful contribution to the solution of the cosmic ray anomalies. At present, these experiments are only suggestive of dark matter particles in the TeV range, not definite. Our goal is to give an account of the general features of the gamma-ray spectrum from annihilation and their imprint on the EGB. For this purpose, our fiducial model with $m_\chi \sim 200$ GeV is adequate. Models with higher masses would shift the energy scale to higher values, but our general conclusions would remain unaltered.

4 GAMMA-RAY LUMINOSITY FROM ANNIHILATION IN HALOES AND SUBHALOES: THE ASTROPHYSICAL FACTOR

In this section we analyse the astrophysical part of the annihilation gamma-ray flux, arising from the clustering of dark matter into haloes and subhaloes across cosmic time. To this end we analyse the dark matter haloes in one of the most recent state-of-the-art cosmological N-body simulations.

Specifically, we use the "Millennium-II" simulation (MS-II) of Boylan-Kolchin et al. (2009) which has the same particle number (2160^3) and cosmological parameters ($\Omega_m = 0.25$, $\Omega_\Lambda = 0.75$, $h = 0.73$, $\sigma_8 = 0.9$ and $n_s = 1$, where Ω_m and Ω_Λ are the contribution from matter and cosmological constant to the mass/energy density of the Universe, respectively, h is the dimensionless Hubble constant parameter at redshift zero, n_s is the spectral index of the primordial power spectrum, and σ_8 is the rms amplitude of linear mass fluctuations in $8\,h^{-1}$Mpc spheres at redshift zero) as the Millennium simulation (MS-I) (Springel 2005) but with a box size that is 5 times smaller, equal to $L = 100\,h^{-1}$Mpc on a side, thus having a mass resolution of $6.89 \times 10^6\ h^{-1}\mathrm{M}_\odot$, 125 times smaller than in MS-I. Typical Milky-Way sized haloes are resolved with several 10^5 particles, while clusters of galaxies have about 50 million particles.

For the dynamical evolution of the MS-II, a fixed comoving gravitational softening length of $\epsilon = 1\,h^{-1}$kpc (Plummer-equivalent) was used. The MS-II was processed on-the-fly to find haloes using a friend-of-friends (FOF) algorithm, followed by a post-processing step to identify gravitationally bound dark matter substructures down to a limit of 20 particles within each group based on the SUBFIND algorithm (Springel et al. 2001). A given FOF halo is decomposed by SUBFIND into disjoint subgroups of self-bound particles. The most massive of these subgroups represents the "main" or "background" halo of a given FOF halo (see Fig. 3 of Springel et al. 2001). For the reminder of this work we will refer to these subgroups as main haloes or simply haloes, and to the rest of the identified subgroups of a given FOF halo as subhaloes of that main halo. SUBFIND also computes several properties for each subgroup; the ones we will use extensively in this work are $V_{\rm max}$ and $r_{\rm max}$, the maximum circular velocity of a (sub)halo and the radius where this maximum is attained. We also use $r_{1/2}$, the radius which encloses half of the mass of a subhalo, and r_{200}, the radius where the mean density of a main halo is 200 times the mean background matter density.

Even with the large particle number available in the MS-II simulation, it is important to note that a direct evaluation of halo luminosities by estimating local dark matter densities at the positions of each simulation particle (for example based on the SPH kernel interpolation technique) would be seriously affected by resolution limitations. This is because most of the emission originates over a tiny radial region, close to the very centre of a halo, where the density is easily underestimated even for otherwise well resolved structures. In fact, it requires of order $10^8 - 10^9$ particles to obtain a converged estimate of the emission from the smooth part of a cuspy dark matter halo in a brute-force approach (Springel et al. 2008). On the other hand, it is numerically *very much easier* to resolve the existence of a halo or subhalo, and to accurately estimate its total mass, as well as its primary structural properties such as $V_{\rm max}$ and $r_{\rm max}$. Our strategy will therefore be to adopt an analytic fit for the density profile of each detected dark matter halo and to predict its expected emission by integrating this profile. In other words, we will use the scaling relation (5) to compute L'_h for main haloes and subhaloes alike. Since $V_{\rm max}$ and $r_{\rm max}$ can be measured reasonably accurately even for poorly resolved haloes, this gives us a reliable accounting for the total emission of all haloes down to a fairly low mass limit. Importantly, we can completely avoid in this way to introduce strong mass-dependent resolution effects in our measurements of luminosity as a function of halo mass.

For simplicity, we shall assume that all haloes have a NFW structure, where the local logarithmic slope of the density profile tends asymptotically to -1 for small radii, even though the Aquarius project, a recent set of simulations aimed at following the formation of MW-sized haloes at different mass resolutions, demonstrated that the Einasto profile provides an even better fit (Navarro et al. 2009), a finding that is also supported by the independent 'GHALO' simulation (Stadel et al. 2009). In the Einasto profile, the local logarithmic slope of the density profile changes with radius according to a power law with exponent α_{sh} (typically called shape parameter). According to the Aquarius project, α_{sh} is of the order $0.16 - 0.17$ and varies from halo to halo (Navarro et al. 2009). Previously, Gao et al. (2008) found a dependence on halo mass for the value of the shape parameter (going from 0.16 for galaxy-haloes to 0.3 for massive clusters). However, for the purposes of our work, the NFW profile is a good enough approximation and using it simplifies comparisons to a number of results in the literature. In any case, we note that using the Einasto profile (with a typical shape parameter of 0.17) instead would increase our results for the fluxes by $\sim 50\%$. This value changes only very slightly over the range of values for α_{sh} found for dark matter haloes. Such an uncertainty on the dark matter density profile is considerably lower than others in our analysis, namely, the photon spectrum from annihilation (see Fig. 2) and the contribution from unresolved haloes and subhaloes (see sections 5.3 and 5.4).

Nevertheless, it is important to take into account the impact of finite numerical resolution in the measured val-

ues of $V_{\rm max}$ and $r_{\rm max}$ for the smallest haloes that can be resolved. As has been shown by Springel et al. (2008), the values of $r_{\rm max}$ are increasingly overestimated for smaller haloes whereas for $V_{\rm max}$ the opposite holds. A partial correction for these numerical effects can be obtained by trying to account for the effect of the gravitational softening ϵ for haloes with values of $r_{\rm max}$ close to ϵ. Assuming adiabatic invariance of orbits between softened and unsoftened versions of the same halo, one obtains to leading order:

$$r'_{\rm max} = r_{\rm max}[1+(\epsilon/r_{\rm max})^2]^{-1}$$
$$V'_{\rm max} = V_{\rm max}[1+(\epsilon/r_{\rm max})^2]^{1/2}, \quad (13)$$

where the primed quantities refer to the case without softening.

In general, the value of $r_{\rm max}$ tends to be much more affected by the softening than $V_{\rm max}$. This can be clearly seen in the upper panel of Fig. 3 where we show the $V_{\rm max}$-$r_{\rm max}$ relation for all main haloes of the MS-II. Note that the relation has some intrinsic scatter, but we here only show the mean values of $r_{\rm max}$ in logarithmic bins of $V_{\rm max}$. The red solid lines show the correlation for different redshifts equal to $z = 0.5$, 1.0, 1.5 , 2.1, 3.1, and 4.9, after the softening correction of Eqs. (13) has been applied, whereas the thicker line is for $z = 0$. The black solid line is an extrapolation of the results found by Neto et al. (2007) at $z = 0$ for the MS-I. There is a clear upwards deviation from the power-law behaviour for haloes with particle number below $N_p \sim 3600$ (corresponding to a mass of $\sim 2.5\times10^{10}\,h^{-1}{\rm M}_\odot$, or $V_{\rm max} \sim 60\,{\rm km\,s^{-1}}$ at $z = 0$). This deviation indicates that the softening correction is only able to correct part of the resolution effects. We can be certain that this is indeed a numerical effect by looking at the corresponding results for the Aquarius haloes (Springel et al. 2008), which demonstrate with simulations of the same initial conditions but drastically different mass resolutions that the $r_{\rm max}$-$V_{\rm max}$ relation is indeed a power law over a large dynamic range, at least for $V_{\rm max}$ as small as $\sim 1.5{\rm km\,s^{-1}}$. This is the case for both, main haloes and subhaloes (see Fig. 26 of Springel et al. (2008)). We note that haloes with $N_p \sim 1000$ or less are affected importantly by two body relaxation. The discrete representation of a dark matter halo with this low number of particles will undergo two-body encounters whereas a real dark matter system with ~ 100 GeV particles is essentially collisionless. Generically, the two-body relaxation process tends to reduce the concentration of objects (e.g. Diemand et al. 2004). We think this is the main mechanism responsible for the upturn shown in Figs. 3 and 7, even though a detailed study of this effect is out of the scope of this work.

Since an overestimate of $r_{\rm max}$ can result in an underestimate of the computed luminosity for a given halo, we further correct the $r_{\rm max}$ values of small haloes phenomenologically in order to allow use of all haloes in the MS-II down to the minimum resolved halo mass of $1.4\times10^8\,h^{-1}{\rm M}_\odot$, and to get the correct mean halo luminosity over the full mass range. For this purpose, we force the values of $r_{\rm max}$ for all haloes with less than 3600 particles to follow the power law

$$r''_{\rm max} = A(z)\left(\frac{V'_{\rm max}}{\rm km\,s^{-1}}\right)^{\alpha(z)} \quad (14)$$

where $A(z)$ and $\alpha(z)$ are the parameters of the power law. These parameters actually depend very mildly on redshift (with $A(0)\approx 0.04$ and $\alpha(0)\approx 1.32$ at $z = 0$). The redshift

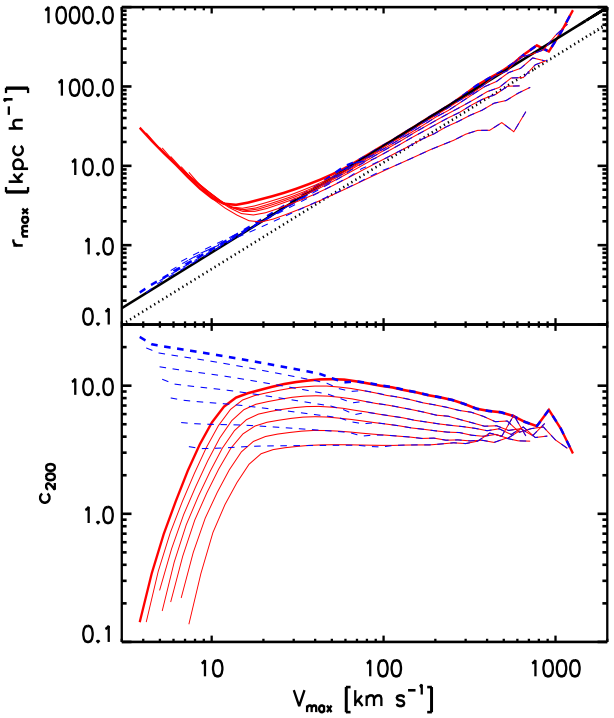

Figure 3. *Upper panel:* Relation between $r_{\rm max}$ and $V_{\rm max}$ for all main haloes in the MS-II at different redshifts. The red solid lines are based on measurements corrected for softening effects with Eqs. (13). The blue dashed lines show the values we adopt for calculating the expected luminosity of a halo; here an additional correction for $r_{\rm max}$ was applied for small haloes such that they extend the power law behaviour measured for well resolved structures. The black solid line is an extrapolation of the results found by Neto et al. (2007) for the MS-I, while the black dotted line is the power law obeyed by subhaloes, see Fig. 7. The thicker lines correspond to $z = 0$, while the rest of the lines are for redshifts: 0.5, 1.0, 1.5, 2.1, 3.1 and 4.9. *Bottom panel:* The relation between concentration c_{200} and $V_{\rm max}$. The line styles and colors are the same as in the upper panel.

dependence can be understood as a change in the mass-concentration relation of haloes, which gets flatter for increasing redshift (Zhao et al. 2003; Gao et al. 2008). We estimate the concentration of the main haloes following the description given in Springel et al. (2008), where a measure of the concentration is obtained in terms of the mean overdensity within $r_{\rm max}$ relative to the critical density $\rho_{\rm crit}$:

$$\delta_V = \frac{\bar\rho(r_{\rm max})}{\rho_{\rm crit}} = 2\left(\frac{V_{\rm max}}{H(z)r_{\rm max}}\right)^2, \quad (15)$$

where $H(z)$ is the Hubble rate as a function of redshift. The overdensity δ_V can be related to the usual concentration parameter $c_{200} = r_{200}/r_s$ of the NFW profile using the characteristic overdensity:

$$\delta_c = \frac{200}{3}\frac{c_{200}^3}{\ln(1+c_{200}) - c/(1+c_{200})} = \frac{\rho_s}{\rho_{\rm crit}} = 7.213\,\delta_V. \quad (16)$$

Using Eq. (16) we can compute c_{200} for a given value of $V_{\rm max}$ and $r_{\rm max}$. The lower panel of Fig. 3 shows the relation between c_{200} and $V_{\rm max}$ for the corrected and uncorrected values of $r_{\rm max}$ as blue dashed and red solid lines, respectively,

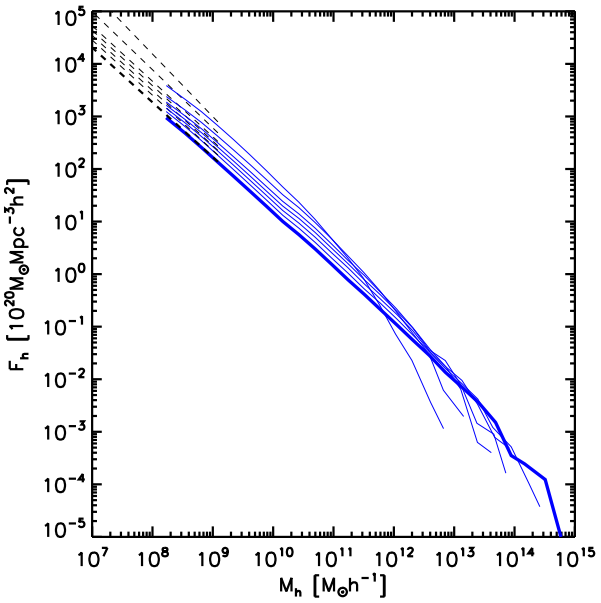

Figure 4. Total luminosity coming from main haloes per differential mass interval as a function of mass. The thin blue lines are for different redshifts as in Fig. 3, while the thick solid line shows the $z = 0$ result. The dashed lines show the run of our extrapolations as discussed in the text.

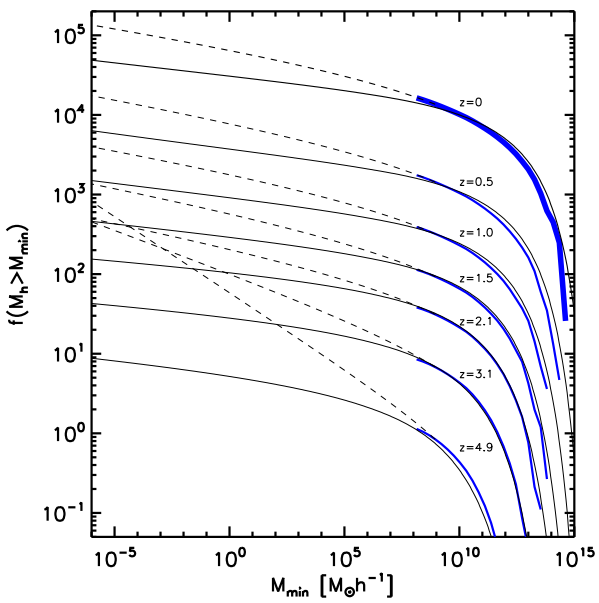

Figure 5. Flux multiplier $f(M_{\rm h} > M_{\rm min})$ for the main haloes in the MS-II as a function of $M_{\rm min}$. The solid-blue and dashed-black lines are analogous to the ones in Fig. 4. The solid-black line is a theoretical estimate as described in the text.

with the redshift increasing from top to bottom. The change in slope of the power law followed by the blue dashed lines is roughly in agreement with the results of Zhao et al. (2003) and Gao et al. (2008).

4.1 Gamma-ray luminosity of haloes down to the damping scale limit

Following the formulation in section 2, we here analyze the flux multiplier for large volumes, Eqs. (6) and (8), for the MS-II. Recall, the flux multiplier gives the ratio of the γ-ray flux coming from all haloes inside the simulated volume with masses larger than a minimum mass $M_{\rm min}$ to the emission produced by a homogeneous distribution of dark matter filling the box of volume V_B with an average density $\bar{\rho}_B$.

We obtain this dimensionless flux multiplier by defining first the function

$$F_h(M_h) = \frac{\sum L_h}{\bar{M}_h \Delta \log M_h}, \qquad (17)$$

where the sum is over all the luminosities L_h of haloes with masses in the logarithmic mass range: $\log M_h \pm \Delta \log M_h/2$, where $\Delta \log M_h$ is a fixed logarithmic bin size; $\bar{M}_h$ is the mean value of the halo mass in the given bin. Using this definition we can approximate Eq. (8) as

$$f(M_h > M_{\rm min}) \sim \frac{1}{\bar{\rho}_B^2 V_B} \int_{M_{\rm min}}^{\infty} \frac{F_h(M_h)}{\ln 10}\, {\rm d}M_h. \qquad (18)$$

In this sense, the function $F_h(M_h)$ is just the total luminosity of haloes in a mass range, per unit mass range. The function $F_h(M_h)$ is shown in Fig. 4 for all main haloes in the MS-II. The different blue lines are for different redshifts, as in Fig. 3.

At intermediate mass ranges, $F_h(M_h)$ is clearly well approximated by a power law:

$$F_h(M_h, z) = A_h(z) M_h^{\alpha_h(z)}. \qquad (19)$$

Our goal is to fit the parameters of this power law so that an extrapolation can be done down to the cutoff mass for neutralinos. For the neutralino mass corresponding to the model we have chosen, the free streaming mass is of the order of $10^{-7}\, h^{-1}{\rm M}_\odot$ (Hofmann et al. 2001), however, acoustic oscillations due to the coupling between cold dark matter and the radiation field in the early Universe, can also produce a damping in the power spectrum of density perturbations (e.g. Loeb & Zaldarriaga 2005). The cutoff mass of the smallest haloes that can be formed is determined by the strongest of these effects. Taking the recent results of Bringmann (2009) (see their Fig. 3), this cutoff mass for $m_\chi = 185$ GeV lies in the range $10^{-9} - 10^{-4}{\rm M}_\odot$. We will take a fiducial value of $10^{-6}\, h^{-1}{\rm M}_\odot$ for our extrapolation, noting that the value of the minimum mass for bound neutralino dark matter haloes is a source of uncertainty in our results.

We obtain the parameters of the power law in Eq. (19) by fitting the function $F_h(M_h)$ between two mass limits, with the lower limit chosen as $M_{\rm lim,min} = 6.89 \times 10^8\, h^{-1}{\rm M}_\odot$, corresponding to haloes with 100 particles (below this number the mass and abundance of haloes is not reliable), and the higher limit set equal to the last logarithmic mass bin with more than 500 haloes, such that uncertainties from counting statistics are avoided. We find that for these mass ranges, the parameters of the power law fits change only slightly with redshift; in fact for $z < 2.1$, $\alpha_h \simeq -1.05$ with less than 2% variation, and $A_h \simeq 6.92 \times 10^{11}$ with less than 50% variation. The black dashed lines in Fig. 4 show the resulting extrapolation of the power law down to $10^7\, h^{-1}{\rm M}_\odot$.

The blue lines in Fig. 5 give results for the flux multiplier, Eq. (18), as a function of $M_{\rm min}$ for the main haloes in the MS-II for different redshifts, as in in Fig. 4. The black dashed lines show the extrapolation of the flux multiplier down to $M_{\rm min} = 10^{-6}\,h^{-1}{\rm M}_{\odot}$ using Eq. (19). The flux multiplier has been previously computed analytically by Taylor & Silk (2003). We follow their procedure and calculate an analytical estimate of $f(M > M_{\rm min})$ for the cosmology corresponding to the MS-II. We first use Eq. (3) to compute the individual flux multiplier $f_h(c_\Delta)$ of an NFW halo with a concentration c_Δ given by the redshift mass-concentration relation, computed as in the analytical model of Eke et al. (2001) and with a choice of $\Delta = 178\,\Omega_m^{0.45} \sim 95$. Using the value of $f_h(c_\Delta)$ we then compute the full flux multiplier based on Eq. (8), assuming a mass function calculated with the formalism of Sheth et al. (2001). The result is included in Fig. 5 with black solid lines.

We see that these analytic estimates roughly agree with the actual numerical results from the MS-II over the resolved mass range. However, small differences in the slope of $f(M > M_{\rm min})$ at the minimum resolved mass range $(1.39 - 6.89 \times 10^8\,h^{-1}{\rm M}_{\odot})$, produce a large difference for the extrapolated values at the damping scale limit, which amounts to a factor of up to $3-5$. We note that for redshifts $z > 2.1$, our extrapolation down to the cutoff mass is not accurate any more and the obtained values are clearly overestimated. This is a reflection of the difficulties to still reliably fit a power law to $F(M)$ at these high redshifts, where the population of haloes over the resolved mass range becomes ever smaller.

Another interesting question that arises from this statistical analysis is: Which mass scale contributes most to the total flux of gamma rays coming from dark matter annihilations? The answer is presented in Fig. 6, which shows the differential cumulative flux, which is really just the logarithmic derivative of the cumulative flux shown in Fig. 5, as a function of the minimum halo mass. From the figure we see that less massive haloes contribute increasingly more to the total gamma-ray flux coming from dark matter annihilation. There is a clear change in behaviour for a given mass scale $M_{\rm min} \sim 10^{14}\,h^{-1}{\rm M}_{\odot}$ at $z = 0$, going down to $M_{\rm min} \sim 10^{12}\,h^{-1}{\rm M}_{\odot}$ at $z = 2.1$. Fig. 6 also reveals an artificial downturn for the minimum mass range resolved $(1.39 - 6.89 \times 10^8\,h^{-1}{\rm M}_{\odot})$. The analytical expectations, shown as black solid lines, qualitatively agree with the results from the simulation. However, the quantitative differences in the extrapolated region are large.

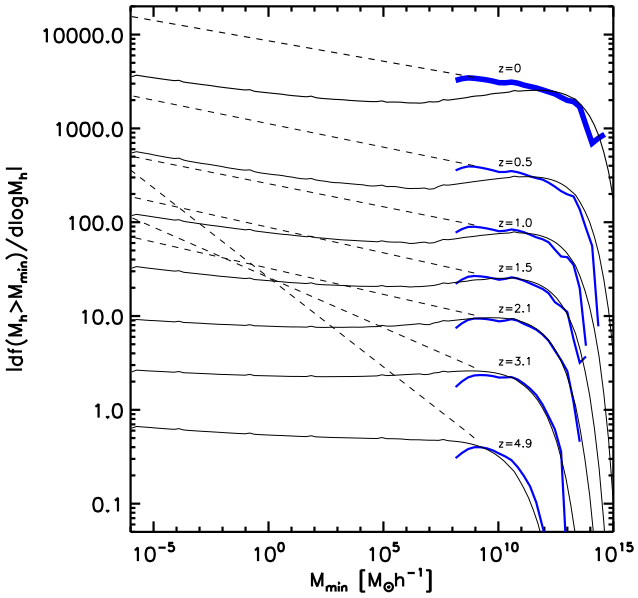

Figure 6. Differential cumulative flux multiplier $|{\rm d}f(M_{\rm h} > M_{\rm min})/{\rm d}\log M_{\rm min}|$ as a function of minimum mass. The line styles and colors are as in Fig. 5.

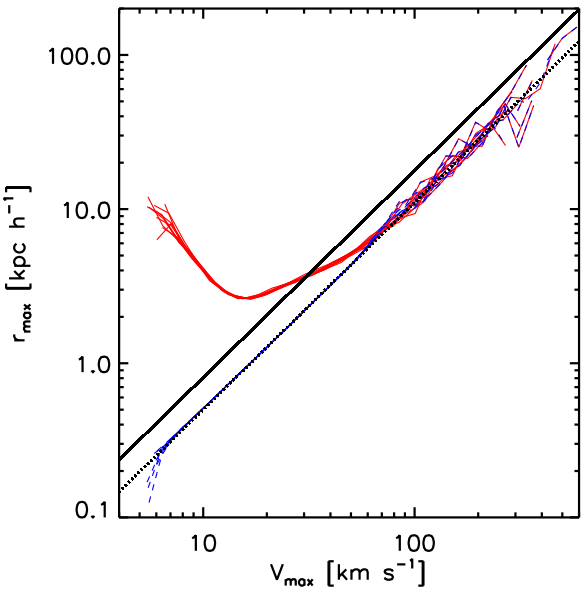

Figure 7. Relation between $r_{\rm max}$ and $V_{\rm max}$ for the subhaloes of the 10 most massive clusters in the MS-II at $z = 0$. These main haloes have V_{max} values in the range $\sim 850 - 1250{\rm kms}^{-1}$. Line styles and colors are as in Fig. 3

4.2 The effects of substructure

Substructures within CDM haloes produce a total γ-ray luminosity which is dominant over the smooth halo component for an external observer (e.g Taylor & Silk 2003). Springel et al. (2008) showed that for a MW halo, substructures with masses larger than $10^5{\rm M}_{\odot}$ within r_{200} emit as much as 76% of the emission of the smooth halo. Also, using their set of simulations of the same halo at different resolutions they extrapolated the contribution from substructures down to masses of $10^{-6}{\rm M}_{\odot}$, at which point they found the total cumulative luminosity to be 232 times larger than the contribution from the smooth halo component.

In this subsection, we analyse the contribution of substructures to the γ-ray flux of the main haloes using as a basis the most massive haloes in the MS-II that contain significant resolved subhaloes and are therefore suitable for such an analysis. To this end we follow an analogous procedure to the one used in the previous subsection.

Fig. 7 shows the $r_{\rm max} - V_{\rm max}$ relation for the population of subhaloes inside the 10 most massive clusters of the MS-II at $z = 0$, the line styles and colors are the same as in

Fig. 3. These clusters have V_{max} values in the range $850 - 1250$ kms^{-1}. The subhaloes follow a very similar power-law behaviour as the population of main haloes in the upper panel of Fig. 3. The slope of the power law is the same, only the normalization is slightly different, a factor of 0.62 lower than for main haloes. This is in agreement with findings obtained for the Aquarius project (Springel et al. 2008).

As for main haloes, we have corrected the values of $r_{\rm max}$ and $V_{\rm max}$ of the subhaloes for softening effects according to Eqs. (13). Also, as for the main haloes, the upturn in the $r_{\rm max} - V_{\rm max}$ relation for small subhaloes clearly indicates an overestimation of $r_{\rm max}$ in this regime due to numerical resolution effects. In order to avoid biasing our results, we hence force the subhaloes in this low-$r_{\rm max}$ low-$V_{\rm max}$ regime to continue to follow the power law defined by the larger, more massive subhaloes:

$$r''_{\rm max} = A_{\rm sub}(z)(V'_{\rm max})^{\alpha_{\rm sub}}, \qquad (20)$$

where $\alpha_{\rm sub}$ has a slight redshift dependence that we can neglect since a value of $\alpha_{\rm sub} \sim 1.34$ fits the mean behaviour of the data for $z < 3$ with an accuracy better than 20%. We find that the value of $A_{\rm sub}(z)$ can be approximated as:

$$A_{\rm sub}(z) \sim 0.023(1+z)^{-1/2}. \qquad (21)$$

As a further consistency check, we have analyzed all main haloes in the MS-II with more than 500 subhaloes, finding that they agree well with the behaviour of the 10 most massive clusters shown in Fig. 7. Thus, all resolved subhaloes in the MS-II with particle number $N_{\rm p} < 3600$ were corrected using Eq. (20).

The contribution of subhaloes, per unit mass range, to the total γ-ray luminosity of their host can be analyzed using the following quantity:

$$F_{\rm sub}\left(\frac{M_{\rm sub}}{M_h}\right) = \left(\frac{M_h}{L_h}\right)\frac{\sum L_{\rm sub}}{\bar{M}_{\rm sub}\Delta\log M_{\rm sub}} \qquad (22)$$

where $M_{\rm sub}$ and $L_{\rm sub}$ are the mass and gamma-ray luminosity of a given subhalo. We have computed $F_{\rm sub}$ for all main haloes in the MS-II with more than 500 subhaloes and found that this quantity can be described by a power law in the intermediate mass range, in a similar way to the function F_h for main haloes:

$$F_{\rm sub}\left(\frac{M_{\rm sub}}{M_h}\right) \sim A_{\rm sub}\left(\frac{M_{\rm sub}}{M_h}\right)^{\alpha_{\rm sub}} \qquad (23)$$

We estimate the parameters of this power law by fitting the results between $M_{\rm sub,min} = 6.89 \times 10^8\, h^{-1}{\rm M}_\odot$, the same lower mass limit used for main haloes, and an upper mass limit given by the most massive logarithmic mass bin with more than 15 subhaloes. Using these two mass limits a power law is found to provide a good fit to the general behaviour in the intermediate mass range for all main halo masses and at different redshifts.

Fig. 8 shows the parameters $A_{\rm sub}$ and $\alpha_{\rm sub}$ of the fit as a function of the mass of the host. The median values for logarithmic mass bins at $z = 0$ are shown with thick black solid lines, the first and third quartiles with thiner black solid lines. The dark grey and light grey lines are for $z = 1.0$ and $z = 2.0$, respectively. The results show almost no dependence of the parameters of the power law fit on the mass of the host and on redshift. For the majority of the

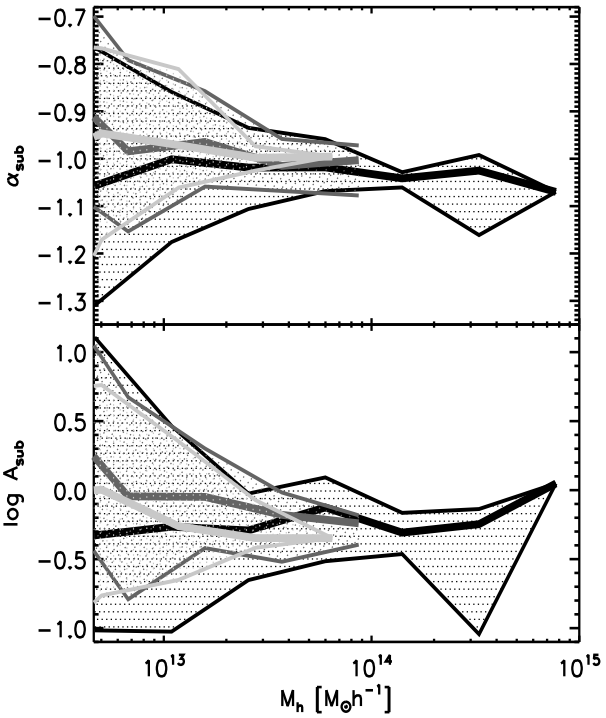

Figure 8. Parameters $\alpha_{\rm sub}$ and $A_{\rm sub}$ from Eq. (23) as a function of main halo mass. The thickest solid lines are the median values for logarithmic mass bins, the dotted regions are within the first and third quartiles. The black, dark grey and light grey lines are for $z = 0$, 1.0 and 2.0, respectively.

cases, these parameters lie in the range:

$$-0.95 \leqslant \alpha_{\rm sub} \leqslant -1.15$$
$$-0.5 \leqslant \log A_{\rm sub} \leqslant 0.1. \qquad (24)$$

For lower host halo masses, the scatter in the parameters for a given mass bin becomes increasingly larger, however. In these cases, the low number of substructures per halo makes the power-law fit less reliable.

We will assume that the power law in Eq. (23) is universal, allowing us to extrapolate the value of $F_{\rm sub}$ down to the damping scale limit. Using the range in Eqs. (24), we can obtain estimates for the maximum and minimum contribution of all substructures to the gamma-ray luminosity of their host halo:

$$f_{\rm sub}(f_{\rm max}, M_h) \sim \frac{1}{L_h}\int_{10^{-6}}^{f_{\rm max}M_h}\left(\frac{L_h}{M_h}\right)\frac{F_{\rm sub}\left(\frac{M_{\rm sub}}{M_h}\right)}{\ln 10}{\rm d}M_{\rm sub}, \qquad (25)$$

where $f_{\rm max}$ is the ratio of the most massive subhalo to the mass of the host. If $\alpha_{\rm sub} \neq -1$ then:

$$f_{\rm sub}(f_{\rm max}, M_h) \sim \frac{A_{\rm sub}\left[(f_{\rm max})^{\alpha_{\rm sub}+1} - \left(\frac{10^{-6}}{M_h}\right)^{\alpha_{\rm sub}+1}\right]}{\ln 10(\alpha_{\rm sub}+1)}. \qquad (26)$$

For the range of values given in Eqs. (24), which reflects the uncertainties in our power law extrapolation, the total luminosity of all substructures in a halo of mass $10^{12}\, h^{-1}{\rm M}_\odot$ lies in the range $f_{\rm sub} \in (2, 1821)$ times the luminosity of the main

halo, bracketing the value of 232 found by Springel et al. (2008) for the Aq-A halo of the Aquarius project.

5 CONTRIBUTIONS TO THE EGB FROM DARK MATTER ANNIHILATION

With the results of the previous sections, we finally concentrate on the main objective of this work, namely, to calculate the contribution of dark matter annihilation to the EGB. Specifically, we are interested in making realistic maps of the expected specific intensity across the sky.

5.1 Simulation of the past light cone

The specific intensity (Eq. 11) describes the total emission from dark matter annihilations integrated over the full backwards light cone along a certain direction. We use the data of the MS-II to fill the whole volume contained in the past-light cone of an observer located at a fiducial position in the box at $z = 0$. As we have 68 simulation outputs in total, we can approximate the temporal evolution of structure growth by using at each redshift along the past light-cone the output time closest to this epoch. To cover all space, we use periodic replication of the simulation box.

However, this periodic replication would introduce strong correlations along the line-of-sight on the scale of the box size, and in particular, would lead to replications of the same structures along certain sight lines. To avoid this problem, we subdivide the backwards light-cone into shells of comoving thickness equal to the boxsize. Within each shell, an independent random rotation and translation is applied to the pattern of boxes that tessellates the shell, as sketched in Fig. 9. This procedure, first used in Carbone et al. (2008), eliminates the unwanted line-of-sight correlations, while at the same time it maintains continuity of the maps in the transverse direction across the sky. As a result, our final maps are free of obvious tessellation artifacts. We note, however, that this procedure can not make up for the missing large scale power on scales larger than the box size itself. Also, it will not be able to eliminate potential excess power in the angular power spectrum on the periodicity scale of the box, as within each shell the simulation box seamlessly tiles the shell. However, the fixed comoving box size translates to a different angular scale in each shell, so that the averaging over many shells usually makes this a small effect.

As discussed earlier, our strategy is not to account for the emission at the level of individual particles, but instead to use entire haloes and subhaloes, allowing us to accurately correct for resolution effects. The list of dark matter particles at each output time is hence replaced by a catalogue of dark matter substructures, each with a known total luminosity and known radial luminosity profile, calculated from their $r_{\rm max}$ and $V_{\rm max}$ values as described earlier, and including a resolution correction for poorly resolved objects. Map-making then becomes a task to accurately accumulate the properly redshifted emission from these structures in discretized representations of the sky. For the pixelization of the sky we use equal area pixels based on the

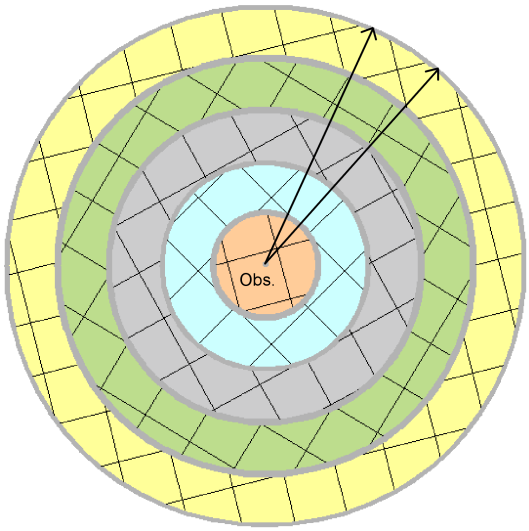

Figure 9. Sketch of the light-cone reconstruction carried out with the periodic MS-II simulation. We subdivide the light-cone into shells of comoving thickness $100\,h^{-1}$Mpc. Within each shell, a coherent randomization of the orientation and translation of the periodic tessellation with the simulation box is carried out, in order to avoid repetition of the same structures along a given line-of-sight and at the same time to maintain continuity in the transverse direction across the sky. The time evolution of cosmic structure is taken into account by using at each position (redshift) along a line-of-sight the closest simulation output time.

HEALPIX[3] tessellation (Górski et al. 2005). All our maps use $N_{\rm pix} = 12 \times 512^2 \sim \pi \times 10^6$ pixels corresponding to an angular resolution of $\sim 0.115^\circ$.

A given pixel in the simulated maps covers a solid angle $\Delta\Omega_{\rm pix}$. Our map-making code computes the average value of the specific intensity within the area subtended by this solid angle by conservatively distributing the emission of each substructure over the appropriate pixels. Combining Eqs. (9) and (11) we can write the relevant sum over all substructures in the light-cone as:

$$I_{\gamma,0}(\Delta\Omega_{\rm pix}) = \frac{1}{8\pi} \sum_{h \epsilon \Delta\Omega_{pix}} L_h w(d_h, r_h) E_{\gamma,0} f_{\rm SUSY}(z_h)|_{E_{\gamma,0}} \tag{27}$$

where the function $w(d_h, r_h)$ is a weight function that distributes the luminosity of a given halo onto the pixels overlapping with the projected "size" (or more precisely the luminosity profile) of the halo; the latter depends on the distance of the observer to the halo d_h and the transverse distance r_h between the halo centre and the centre of the pixels it touches. Except for structures that are very nearby, the high central concentration of the emission of a subhalo and the limited angular resolution of our maps give most subhaloes the character of unresolved point sources. It therefore makes little difference in practice if the transverse luminosity profile of a subhalo, a ρ^2-weighted projection of a NFW profile, is replaced with an SPH-like kernel function in 2D with radius equal to the halo's half-mass radius $r_{1/2}$. However, it is important to guarantee that the sum of the weights

[3] The HEALPIX software package is available at http://healpix.jpl.nasa.gov

$w(d_h, r_h)$ associated with all pixels that overlap with a given substructure 'add up to unity', i.e. that the total emission of the halo is represented in the map in a conservative fashion. Our map-making code guarantees this property. For performance reasons, the code also uses a tree-based approach to quickly find all subhaloes (and also any of their periodic images, if appropriate) that overlap with a given line of sight.

For the purpose of extending the predictions of our maps down to the damping scale limit of neutralinos ($\sim 10^{-6}\mathrm{M}_\odot$), we will incorporate the results of section 4 by dividing the maps into separate components: (i) the contribution of *resolved haloes and subhaloes* with a minimum mass of $6.89\times10^8\ h^{-1}\mathrm{M}_\odot$ (called "ReHS" in the following); (ii) the contribution of *unresolved main haloes* with masses in the range $1.0\times10^{-6} - 6.89\times10^8\ h^{-1}\mathrm{M}_\odot$ (referred to as "UnH"); and finally, (iii) the contribution of *unresolved subhaloes* in the same mass range as in the case (ii) (component "UnS").

5.2 Resolved haloes and subhaloes (ReHS)

In Fig. 10, we show full sky maps of the the γ-ray emission of all main haloes and subhaloes that are detected in the MS-II; this corresponds to an essentially perfectly complete sample of all haloes above a mass limit of $6.89\times10^8\ h^{-1}\mathrm{M}_\odot$. In the top panel of Fig. 10, a partial map at low redshift (corresponding to the first shell at $z = 0$ of depth $50\,h^{-1}$Mpc) is shown in order to illustrate typical foreground structure, whereas the bottom panel gives an integrated map out to $z = 10$, which is approximately the full EGB from annihilation. The maps in Fig. 10 are for $E_{\gamma,0} = 10\,\mathrm{GeV}$, where $E_{\gamma,0}$ is the photon energy measured by the observer (i.e. the emission energy of the photons is $E_\gamma = (1+z)E_{\gamma,0}$). In the color scale used for the maps, red corresponds to the highest and black to the lowest values of the specific intensity, respectively.

5.3 Unresolved haloes (UnH)

The maps shown in Fig. 10 are complete down to the minimum mass in the MS-II that we can trust, $\sim 6.89\times10^8\ h^{-1}\mathrm{M}_\odot$. In order to make a prediction of the full EGB coming from dark matter annihilations, we extrapolate the γ-ray flux to account for the contribution of all missing dark matter haloes down to the cutoff mass $10^{-6}\ h^{-1}\mathrm{M}_\odot$. For this purpose we use the results found in section 4 on the universal power law behaviour of the functions $F_h(M_h)$ and $F_{\rm sub}(M_{\rm sub}/M_h)$.

The way we incorporate this contribution in the γ-ray maps is the following. We assume that the EGB radiation from the missing haloes in the mass range $10^{-6}\ h^{-1}\mathrm{M}_\odot$ to $\sim 6.89\times10^8\ h^{-1}\mathrm{M}_\odot$ is distributed on the sky in the same way as the one from the smallest masses we can resolve in the simulation, which we adopt as the mass range between $1.4\times10^8\ h^{-1}\mathrm{M}_\odot$ and $\sim 6.89\times10^8\ h^{-1}\mathrm{M}_\odot$ (haloes with 20 to 100 particles). This assumption can be justified by the clustering bias of dark matter haloes that appears to approach an asymptotic constant value for low halo masses (e.g Boylan-Kolchin et al. 2009). Hence, we compute the value of a boost factor b_h with which each resolved halo in the mass range $1.4 - 6.89\times10^8\ h^{-1}\mathrm{M}_\odot$ needs to be multiplied such that the luminosity of the unresolved main haloes is accounted for as well. Using the power law behaviour of $F_h(M_h)$ and $f(M_h > M_{\rm h,min})$, Eqs. (19) and (18), we find that:

$$b_h = \frac{f(10^{-6}\ h^{-1}\mathrm{M}_\odot, 6.89\times10^8\ h^{-1}\mathrm{M}_\odot)_a}{f(1.4\times10^8\ h^{-1}\mathrm{M}_\odot, 6.89\times10^8\ h^{-1}\mathrm{M}_\odot)_{\rm sim}} \sim 60, \tag{28}$$

where b_h is given by the ratio of the flux multipliers computed analytically, between the cutoff mass limit and the 100 particle limit, and computed within the simulation in the last resolved mass range (20-100 particles). We find that b_h is nearly independent of redshift up to the highest redshift we can reliable measure the power law $F_h(M_h)$, that is for $z < 2.1$.

5.4 Unresolved subhaloes (UnS)

To add the contribution of unresolved substructures to the γ-ray maps, we first assume that the identified subhalo population is complete down to a mass limit of $M_{\rm sub} = 6.89\times10^8\ h^{-1}\mathrm{M}_\odot$. Below this mass we compute luminosities using the formulas presented in section 4.2, separating the way we add this contribution in two cases.

In the case of resolved main haloes with more than 100 particles, we simply use Eq. (26) with $f_{\rm max}M_h = 6.89\times10^8\ h^{-1}\mathrm{M}_\odot$ if the main halo has subhaloes, and $f_{\rm max} = 0.05$ otherwise. For the former case we distribute the extra luminosity coming from unresolved substructures among the subhaloes of the main host, assuming in this way that unresolved subhaloes are distributed in the same way as the resolved ones. For the latter, the extra luminosity is given to the main background subhalo. We note that in this case the particular value of $f_{\rm max}$ has little impact in Eq. (26) since $M_h \geqslant 6.89\times10^8\ h^{-1}\mathrm{M}_\odot$ and thus, the right-hand side of the term in brackets is dominant for $\alpha_{\rm sub} < -1$; for the extreme value of $\alpha_{\rm sub} = -0.95$, values of $f_{\rm max}$ between 0.005 and 0.5 give variations of $f_{\rm sub}$ smaller than 3.5%. We use $f_{\rm max} = 0.05$ since this is a typical value in the MS-II.

For the second case of all main haloes, resolved and unresolved, with masses less than $6.89\times10^8\ h^{-1}\mathrm{M}_\odot$ we use the following strategy. Since in the last subsection we described how to get the total luminosity coming from all main haloes with masses between the damping scale limit and $6.89\times10^8\ h^{-1}\mathrm{M}_\odot$, we can compute the boost factor $b_{\rm sub}$ for which this luminosity needs to be multiplied in order to include the full contribution of all subhaloes of the main haloes in this mass range:

$$b_{\rm sub} = \frac{\mathfrak{f}_{\rm boost}(10^{-6}\ h^{-1}\mathrm{M}_\odot, 6.89\times10^8\ h^{-1}\mathrm{M}_\odot)}{\mathfrak{f}_{\rm no-boost}(10^{-6}\ h^{-1}\mathrm{M}_\odot, 6.89\times10^8\ h^{-1}\mathrm{M}_\odot)} \tag{29}$$

where $\mathfrak{f}_{\rm no-boost}$ is given by:

$$\mathfrak{f}_{\rm no-boost}(10^{-6}\ h^{-1}\mathrm{M}_\odot, 6.89\times10^8\ h^{-1}\mathrm{M}_\odot) \approx \int_{10^{-6}}^{6.89\times10^8} \frac{F_h(M_h)}{\ln 10}\,\mathrm{d}M_h \tag{30}$$

and $\mathfrak{f}_{\rm boost}$ can be written as:

$$\mathfrak{f}_{\rm boost}(10^{-6}\ h^{-1}\mathrm{M}_\odot, 6.89\times10^8\ h^{-1}\mathrm{M}_\odot) \approx \int_{10^{-6}}^{6.89\times10^8} [1 + f_{\rm sub}(f_{\rm max}, M_h)]\frac{F_h(M_h)}{\ln 10}\,\mathrm{d}M_h. \tag{31}$$

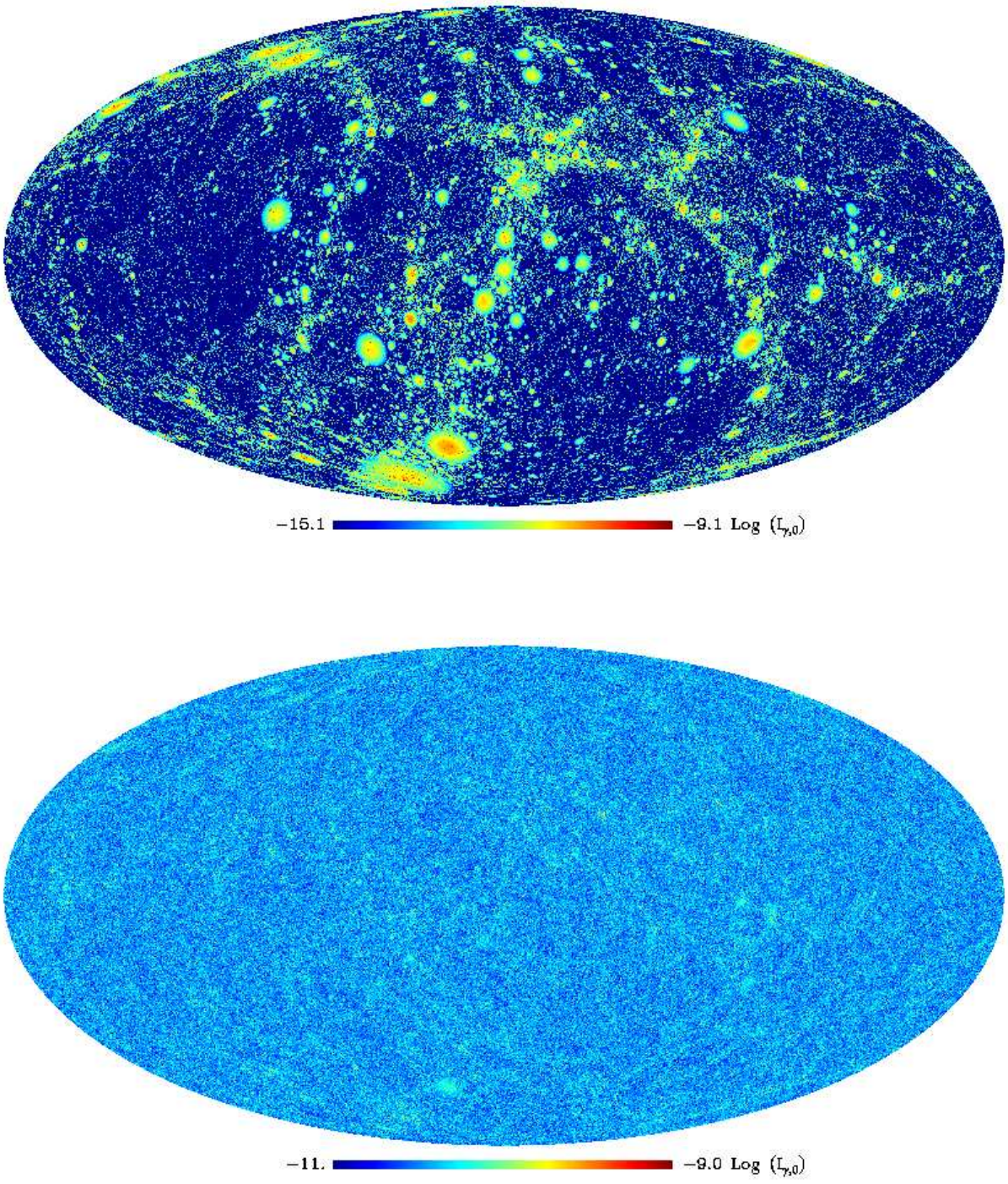

Figure 10. *Upper panel:* One of the partial maps ($z = 0$) showing the cosmic γ-ray background produced by dark matter annihilation. The color scale gives a visual impression of the values of the specific intensity for each pixel in the map; the red color corresponds to the highest values of specific intensity. The observed energy of the simulated γ-ray radiation is 10 GeV, and the benchmark point L as described on Table 1 was used as input for the supersymmetric model. *Lower panel:* Co-added map showing the full γ-ray sky map from dark matter annihilation integrated out to $z = 10$.

After using Eqs. (18) and (19) we can write:

$$b_{\rm sub} = 1 + \frac{A_{\rm sub}}{\ln 10(\alpha_{\rm sub}+1)}\Bigg\{ f_{\rm max}^{\alpha_{\rm sub}+1} - (10^{-6})^{\alpha_{\rm sub}+1} \left(\frac{\alpha_h+1}{\alpha_h-\alpha_{\rm sub}}\right)\frac{(6.89\times10^8)^{\alpha_h-\alpha_{\rm sub}} - (10^{-6})^{\alpha_h-\alpha_{\rm sub}}}{(6.89\times10^8)^{\alpha_h+1} - (10^{-6})^{\alpha_h+1}}\Bigg\} \quad (32)$$

We found that $b_{\rm sub}$ is roughly independent of redshift. Using the values of $\alpha_h = -1.05$, $A_{\rm sub}$, $\alpha_{\rm sub}$ determined earlier, we obtain $b_{\rm sub} \approx 2-60$. We shall take the extreme values of this range in the following presentation of our results, as these minimum and maximum values reflect the uncertainties in our extrapolation and should bracket the true result.

5.5 Isotropic and anisotropic components of the EGB from dark matter annihilation

The upper panel of Fig. 11 shows the mean value of the specific intensity $\Delta I_{\gamma,0}$ divided by the comoving thickness of the shell (equal to $100\,h^{-1}$Mpc, except for the map at $z = 0$ where the shell is half as thick) at $E_{\gamma,0} = 10\,$GeV for our partial sky maps as a function of redshift. Recall that each partial map represents the total specific intensity in a shell of constant comoving thickness, so this provides information about where the signal is coming from. The black line is for the ReHS case, while the dashed line is for main haloes only (resolved and unresolved, including the boost factor $b_h = 60$). The remaining lines are for the resolved and unresolved main haloes and their subhaloes, boosted to include the contribution of structures all the way down to the damping scale limit; here the light grey line is for the "minimum boost" with $b_{\rm sub} = 2$ whereas the dark grey line is for the "maximum boost" with $b_{\rm sub} = 60$, but both include the boost $b_h = 60$ for unresolved main haloes.

In all cases, the contribution from partial maps up until $z \sim 1$ is almost constant, indicating that the increasing number of sources for shells at higher redshifts, due to the larger volume seen behind each pixel, is approximately compensated by the distance factor and the spectral effects from the cosmological redshifting and the intrinsic variation of the emission spectrum, as described by $f_{\rm SUSY}$ (see Fig. 2).

The lower panel of Fig. 11 shows the accumulated mean value of the specific intensity as a function of redshift. This clearly shows that the most relevant contributions come from maps up to $z \sim 2$. For higher redshifts, the partial maps contribute less than 5% to the total. Overall, applying the maximum boost increases the mean value of $I_{\gamma,0}$ of the ReHS case by three orders of magnitude. However, it is important to note that Fig. 11 depends on the observed energy $E_{\gamma,0}$, and more specifically on the spectral shape of the factor $f_{\rm SUSY}$ in the energy range $E_{\gamma,0} - E_{\gamma,0}(1+z_{\rm max})$, where $z_{\rm max}$ is the largest redshift considered, in our case $z_{\rm max} = 10$. For most energies, the $f_{\rm SUSY}$ spectrum is monotonically decreasing. In these regions, the dependence on $I_{\gamma,0}$ with redshift will have the generic form shown in Fig. 11. However, at the highest energies the shape is expected to change dramatically due to the importance of Internal Bremsstrahlung and/or of monochromatic lines (see Fig. 2) close to the rest mass energy of the dark matter particle. Such an effect is clearly visible in the black dotted line in Fig. 11, which is the ReHS case for an energy of 100 GeV and features a bump

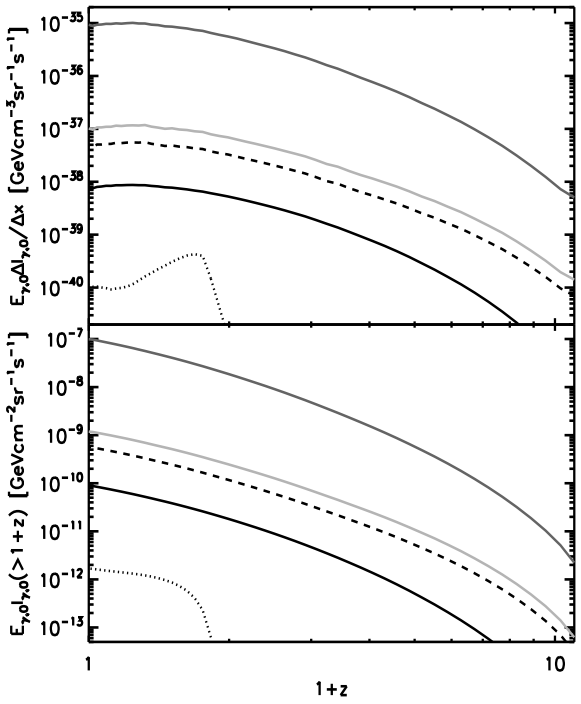

Figure 11. *Upper panel:* Mean annihilation intensity per comoving shell thickness, $\Delta I_{\gamma,0}/\Delta x$, as a function of redshift for individual partial maps. The solid black line is for resolved haloes and subhaloes. The dashed black line is for main haloes only, resolved and unresolved down to the cutoff mass using a boost factor $b_h = 60$. The light grey and dark grey solid lines show the contribution of all components, resolved and unresolved haloes and subhaloes, boosted with the extreme values in the interval $b_{\rm sub} = 2 - 60$. All lines are for $E_{\gamma,0} = 10\,$GeV, except for the black dotted line which is for the ReHS component with $E_{\gamma,0} = 100\,$GeV. *Lower panel:* The same as the upper panel but for the accumulated intensity, $I_{\gamma,0}(>1+z)$.

in the redshift distribution, a reflection of the importance of IB at the highest energies.

The angular power spectrum of the EGB is an important tool to study the statistical properties of its anisotropy on the sky. In fact, certain classes of γ-ray sources are expected to exhibit different power spectra, making this a potential means to identify the origin of the unresolved EGB. If we decompose the relative deviations of the EGB around its mean into spherical harmonics with coefficients a_{lm},

$$\Delta_{I_{\gamma,0}}(\theta,\phi) = \frac{I_{\gamma,0}(\theta,\phi) - \langle I_{\gamma,0}\rangle}{\langle I_{\gamma,0}\rangle} = \sum_{l=0}^{\infty}\sum_{m=-l}^{m=l} a_{lm}Y_{lm}(\theta,\phi), \quad (33)$$

then the angular power spectrum is defined by the real numbers

$$C_l = \frac{1}{2l+1}\left(\sum_m |a_{lm}|^2\right). \quad (34)$$

For small angular scales (i.e. large l), the variance of $\Delta_{I_{\gamma,0}}$ per unit decade in l can be connected directly to the C_l's

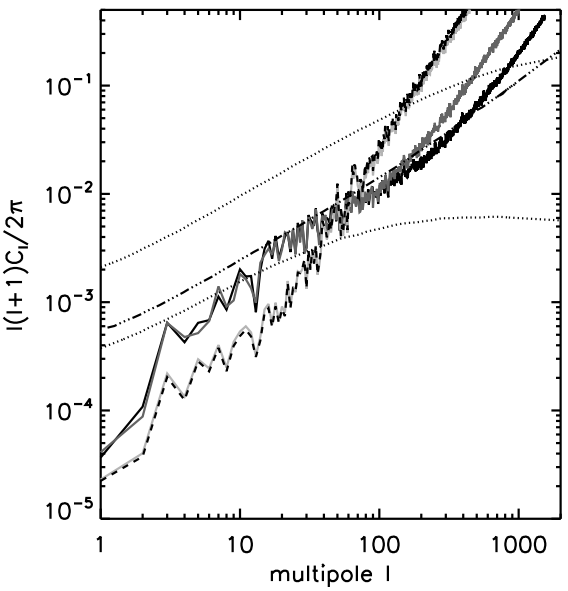

Figure 12. Angular power spectrum of the EGB produced by dark matter annihilation as a function of the multipole l for $E_{\gamma,0} = 10\,\mathrm{GeV}$. The solid black line is for resolved haloes and subhaloes. The dashed black line is for main haloes only, resolved and unresolved down to the cutoff mass using a boost factor $b_h = 60$. The light grey and dark grey solid lines show the contribution of all components, resolved and unresolved haloes and subhaloes, boosted with the extreme values in the interval $b_{\rm sub} = 2 - 60$. The dotted lines show the predictions from Ando et al. (2007b) for a subhalo-dominant contribution with and without considering tidal destruction (lower and upper dotted lines), respectively. The dash-dotted line shows the case where the main halo dominates the signal according to the same study.

through

$$\frac{\mathrm{d}\langle\Delta^2_{I_{\gamma,0}}\rangle}{\mathrm{dln}\ l} \propto l^2 C_l. \qquad (35)$$

In Fig. 12, we show the angular power spectrum $l(l+1)C_l/2\pi$ as a function of the multipole l, at an observed energy of $E_{\gamma,0} = 10\,\mathrm{GeV}$, for all the cases discussed in Fig. 11. At large scales, $l \lesssim 10$, the power spectrum is related to the clustering of dark matter haloes. All cases have the same shape on these scales. However, when only the main halo contribution to the EGB is considered (dashed black line), the normalization is lower because most of the γ-ray signal comes from low mass haloes that are less clustered (biased) than more massive haloes; recall that in this case we extrapolate the signal down to the cutoff mass by assuming that the unresolved main haloes are clustered in the same way as the least massive resolved haloes in the MS-II.

The light grey line in Fig. 12, corresponding to the full extrapolation including subhaloes but with the minimal boost $b_{\rm sub} = 2$, has exactly the same power spectrum than the case with main haloes only, at all scales. This is because the signal from main haloes is dominant in this case, and subhaloes have a negligible effect. In contrast, in the case where subhaloes have a significant contribution mediated by $b_{\rm sub} = 60$ (dark grey line), the normalization is larger at small scales because the signal is dominated by subhaloes belonging to the most massive haloes, and the latter are strongly clustered.

As the angular scale decreases, $l > 10$, the power spectrum depends more and more on the internal structures of haloes. For the cases where substructures are ignored or are negligible (dashed-black and light grey lines), the slope becomes steeper, with a slope close to 2. The power spectrum for the cases where substructures are relevant (dark grey and black solid lines) behaves differently, however. In the range $l \in [20, 100]$, it becomes slightly shallower, i.e. the signal is slightly more isotropic in this regime. This is probably produced by the distribution of substructure within the biggest haloes. Contrary to the strong central concentration of the matter in a halo, the number density profile of subhaloes is considerably shallower than a NFW profile and produces a luminosity profile in projection which is essentially flat (Springel et al. 2008). This effect continues until $l \sim 200$ where the power spectrum becomes dominated by the low-mass main haloes. The corresponding upturn happens at smaller scales for the case corresponding to the black line because the substructures in the most massive haloes remain important for a larger angular range, whereas for the case of the dark grey line, the low-mass unresolved main haloes start to dominate earlier.

The dash-dotted and dotted lines in Fig. 12 were taken from the analysis of Ando et al. (2007b). They were obtained under the assumption of a Sheth-Tormen mass function (Sheth et al. 2001), a halo bias according to the model of Mo & White (1996), and a NFW main halo density profile with a concentration given by the mass-concentration relation found by Bullock et al. (2001). Subhaloes were incorporated through a halo occupation distribution model, where the number of subhaloes in each main halo, $\langle N_{\rm sub}|M_h\rangle$, is assumed to depend only on the mass of the host according to $\langle N_{\rm sub}|M_h\rangle \propto M_h^{\beta}$. The upper dotted line in Fig. 12 is for $\beta = 1.0$ and the lower dotted line for $\beta = 0.7$; in these cases subhaloes dominate completely the signal. The subhaloes are assumed to be distributed with a NFW radial profile inside the main halo. Since they dominate the signal, the total gamma-ray luminosity (halo + subhaloes) is effectively tracing the density of dark matter instead of the density squared as expected for a smooth halo with no substructures. This case is represented with a dash-dotted line in Fig. 12. In all three cases only the contribution of haloes down to a minimum mass of $10^6\mathrm{M}_\odot$ is taken into account.

There are several approximations used by Ando et al. (2007b) that we believe may be the cause of the differences between their results and ours. In our case, the clustering of dark matter haloes is given directly by the simulations instead of by an approximate halo model. This introduces differences that can only be quantified by a direct comparison of the power spectrum of haloes used by Ando et al. (2007b) and the one in the MS-II. Such a comparison is out of the scope of this paper. We need to mention however, that our simulated maps have a deficiency of power at the largest angular scales due to the lack of comoving scales larger than the simulation box (100 Mpc/h). This is a problem already pointed out by Carbone et al. (2008) that used a similar map-making procedure, and is probably the main reason for the disagreement between the results of Ando et al. (2007b) and ours on the large scale regime.

On the other hand, while we do assume a NFW pro-

file, the concentration of each halo is given by its scaling properties (see Eqs. 15 and 16), whereas Ando et al. (2007b) uses the mass-concentration fitting relations found by Bullock et al. (2001). This fitting formulae agree well with simulations at $z = 0$ but strongly disagree at higher redshift. They predict a relatively strong correlation between concentration and mass, contrary to simulations where this correlation gets flatter for higher redshifts. This difference contributes to the discrepancy between our results and those of Ando et al. (2007b) in the small scale regime. Finally, an important disagreement is expected due to the treatment of subhaloes. The model used by Ando et al. (2007b) produces a shallower power spectrum at small scales since the gamma-ray luminosity of a halo is effectively given by the density of dark matter instead of by the square of the density. In simulations, the radial distribution of subhaloes is considerably shallower towards the centre than a NFW profile due to tidal striping (e.g. Diemand et al. 2008; Springel et al. 2008). Near the halo centre our expectation is that the signal will be dominated by the smooth component rather than by substructures. This is an effect that contributes to make our power spectrum steeper at the smaller scales than the one obtained by Ando et al. (2007b).

5.6 Energy dependence

So far we have restricted our analysis to an observed γ-ray energy of 10 GeV. In the following we study how the isotropic and anisotropic components of the γ-ray maps change with photon energy. The black solid line in Fig. 13 shows the energy spectrum of the mean annihilation intensity $I_{\gamma,0}$ for the case of the maximum boost $b_h = 60$, $b_{\rm sub} = 60$ (corresponding to the dark grey line in Fig. 11). For simplicity we refrain from showing the other cases explicitly as they differ only in their normalization (for example, the minimum boost case with $b_{\rm sub} = 2$ simply lies 2 orders of magnitude lower). The solid circles with error bars are observational measurements taken by the satellite EGRET after removal of the galactic foregrounds (Strong et al. 2004). There are several sources other than DM annihilation that contribute to the EGB in the range of energies shown in Fig. 13; blazars and cosmological structure formation shocks are among the most important ones. In Fig. 13, we include the contribution to the EGB from the blazar model introduced by Kneiske & Mannheim (2008) (dashed line) that explains most of the signal for energies lower than 1 GeV. However, there seems to be an excess of γ-ray flux observed in the EGB for energies larger than 1 GeV that can not be readily explained by known astrophysical sources (Ong 2006). Interestingly, the γ-ray spectrum produced by dark matter annihilation has the right shape to fit the observed values in this energy range, even though this could of course be a coincidence. Our maximum boost scenario is in any case still too low (by about an order of magnitude) to explain the dominant component of the EGB in this energy range, and an additional boost factor would be needed to explain this signal, if confirmed, with DM annihilation. An improved and more precise measurement of the energy spectrum will be made by FERMI very soon, so there is hope that this issue will become clearer in the near future. We note that completing and improving the measurements for high energies $E_{\gamma,0} > 20$ GeV is of key importance since the

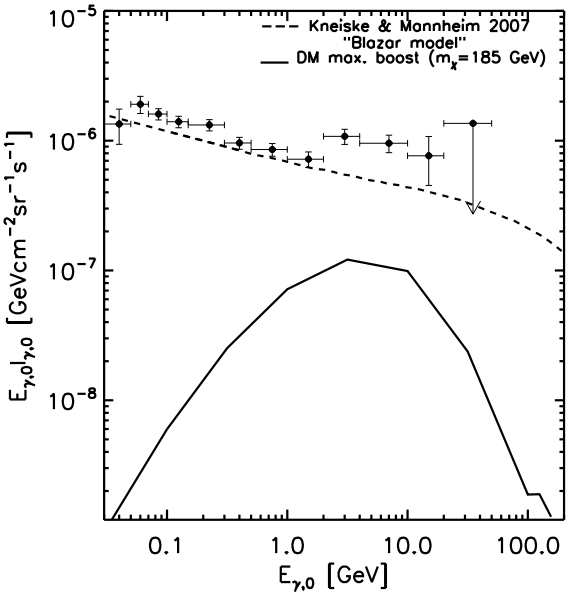

Figure 13. Mean annihilation intensity $E_{\gamma,0}I_{\gamma,0}$ as a function of the observed energy for the maximum boost case, $b_h = 60$, $b_{\rm sub} = 60$. The observational values and the error bars come from the EGRET satellite, as presented by Strong et al. (2004). The "blazar model" given by Kneiske & Mannheim (2008) is shown as a dashed line.

DM annihilation spectrum is expected to drop off sharply at such higher energies, making this an important discriminant against other types of sources.

The presence of a secondary bump at the highest energies, $E_{\gamma,0} \sim 125$ GeV is a consequence of IB effects that become important at these energies. The relevance of this effect depends on the specific parameters chosen for the mSUGRA model (see Fig. 2), but its detection in the isotropic component of the EGB is generically less likely than identifying the primary bump.

Fig. 14 shows the ratio of the power spectrum C_l for different energies to the power spectrum at 10 GeV as a function of the multipole l. The lines are labeled in the left of the figure according to the energy of the map in GeV. For $E_{\gamma,0} \in (0.1, 30)$ GeV there is generally an increase of power for increasing energy, a feature already pointed out by Ando & Komatsu (2006). Whereas overall the variations of the ratio C_l/C_{10} for these low-intermediate energies are small, there are some differences at intermediate to small scales that have important consequences, as we discuss below. For the higher energies, $E_{\gamma,0} \in (100, 156)$ GeV, the signal originates completely at relatively low redshifts. For example at $E_{\gamma,0} = 100$ GeV, *all* the signal comes from $z < 1.0$ (see Fig. 11) since the $f_{\rm SUSY}$ spectrum has a sharp cut-off at the neutralino mass, 185 GeV. The contribution of IB to the photon spectrum is dominant at these energies.

We note that there is a prominent peak in the power spectra for energies 100 and 125 GeV, at $l = 100$ and $l = 60$, respectively. This peak is in fact a spurious effect related to the periodicity across the sky that is present within a given shell (partial map). Since we are working with only one simulation (MS-II) with a finite box size of 100 h^{-1}Mpc, we are

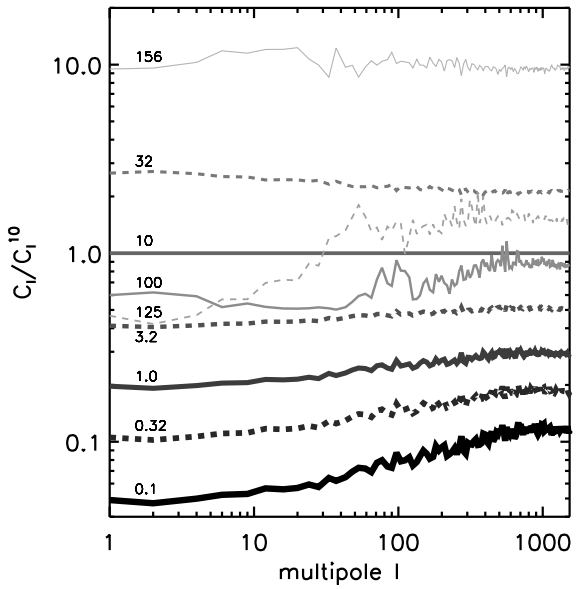

Figure 14. Ratio of the angular power spectrum of the EGB produced by dark matter annihilation at different energies to the one at $E_{\gamma,0} = 10\,\mathrm{GeV}$ (Fig. 12). The lines are labeled according to their respective energy in GeV. They appear in a grey scale going from black to light grey, and with decreasing thickness, for increasing energy. The line styles alternate between solid and dashed for consecutive energies.

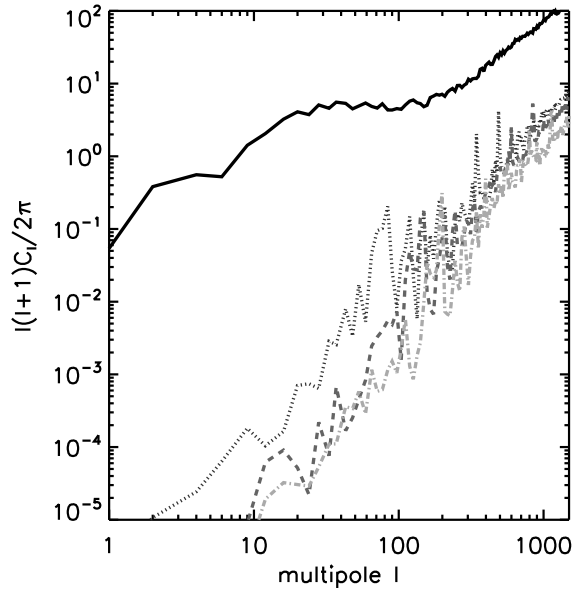

Figure 15. Angular power spectrum of the EGB for different partial maps, i.e. for the volume contained in a shell of comoving thickness $100\,h^{-1}$Mpc at a given redshift, for the sky map at observed energy $E_{\gamma,0} = 10\,\mathrm{GeV}$. The black solid, dark grey dotted, medium grey dashed and light grey dash-dotted lines are for $z = 0$, 0.5, 1.0, and 1.5 respectively.

inevitably affected by the periodicity of the replicas within a given shell. For a particular shell, this periodicity introduces a mild correlation at an angular scale determined by the comoving distance from the observer to the shell and the transverse box size of $100\,h^{-1}$Mpc. This correlation is largely averaged out for the full line of sight integration, as the relevant angular scale changes with redshift. However, for the highest energies, the bump in the spectrum of f_{SUSY} maximizes the contribution from a particular emitted energy, which in turn translates into a particular redshift (see Fig. 11) that contributes most prominently. As a result, the angular correlation from the periodicity corresponding to this particular redshift is particularly strong, and remains visible in the final power spectrum.

To make this effect more evident we show in Fig. 15 the angular power spectrum of different partial maps (i.e. single shells of comoving thickness $100\,h^{-1}$Mpc along the line of sight), for an observed energy of $E_{\gamma,0} = 10\,\mathrm{GeV}$ (to show the periodicity effect, the choice of energy is not important). The black solid, dark grey dotted, medium grey dashed and light grey dash-dotted lines are for shells at $z = 0$, 0.5, 1.0, and 1.5, respectively. Clearly, there are peaks at certain values of l for the red, green, and blue lines. The values of the multipole l where the peaks occur correspond to angular scales that are closely related to the boxsize at the distance of the shells. Specifically we find 104.4, 116.7, 99.9 h^{-1}Mpc for 0.5, 1.0, and 1.5, respectively. This effect is not present at $z = 0$, since the first shell, with a depth of $50\,h^{-1}$Mpc, encloses a volume too small to contain the full box.

Another important result that we obtain from the analysis of the power spectra is that there are differences in the shape of the power spectra in Fig. 14 for different energies. We can exploit these differences and enhance the power at small or large angular scales by taking the *ratio of sky maps at different energies*. In particular, the case of the energies $E_{\gamma,0} = 0.1\,\mathrm{GeV}$ and $E_{\gamma,0} = 32\,\mathrm{GeV}$ (black-solid and red-dotted lines, respectively) is notable since these energies are free from periodicity effects and when combined they can enhance the intermediate to large angular scales. The upper panel of Fig. 16 shows the total sky maps for $E_{\gamma,0} = 0.1\,\mathrm{GeV}$ and $E_{\gamma,0} = 32\,\mathrm{GeV}$ in the left and right, respectively, smoothed with a Gaussian beam with a FWHM of 5°. Both maps show only small anisotropies, with the exception of a couple of prominent structures. The sky map in the lower left panel is the ratio of the two maps; it clearly enhances the signal of nearby structures. This is even more convincing by looking at the nearest partial map at $z = 0$ for $E_{\gamma,0} = 0.1\,\mathrm{GeV}$ shown in the lower right corner of Fig. 16. Most of the prominent dark matter structures that can be seen in this map are also clearly present in the map with the energy ratio. We conclude that the γ-ray sky maps that the FERMI satellite will obtain at different energies could be used to construct difference maps which may then show enhanced correlations with nearby cosmic large-scale structure.

In our results, we have neglected the interactions between the gamma-ray photons produced by annihilation and the lower energy photons from intervening starlight produced in galaxies. This interaction enters effectively as an absorption term in the specific intensity in Eq. (11) due to pair production, and is usually parameterised by an exponential factor $e^{-\tau(z,E_{\gamma,0})}$ (e.g. Ando & Komatsu 2006; Fornasa et al. 2009). Fornasa et al.

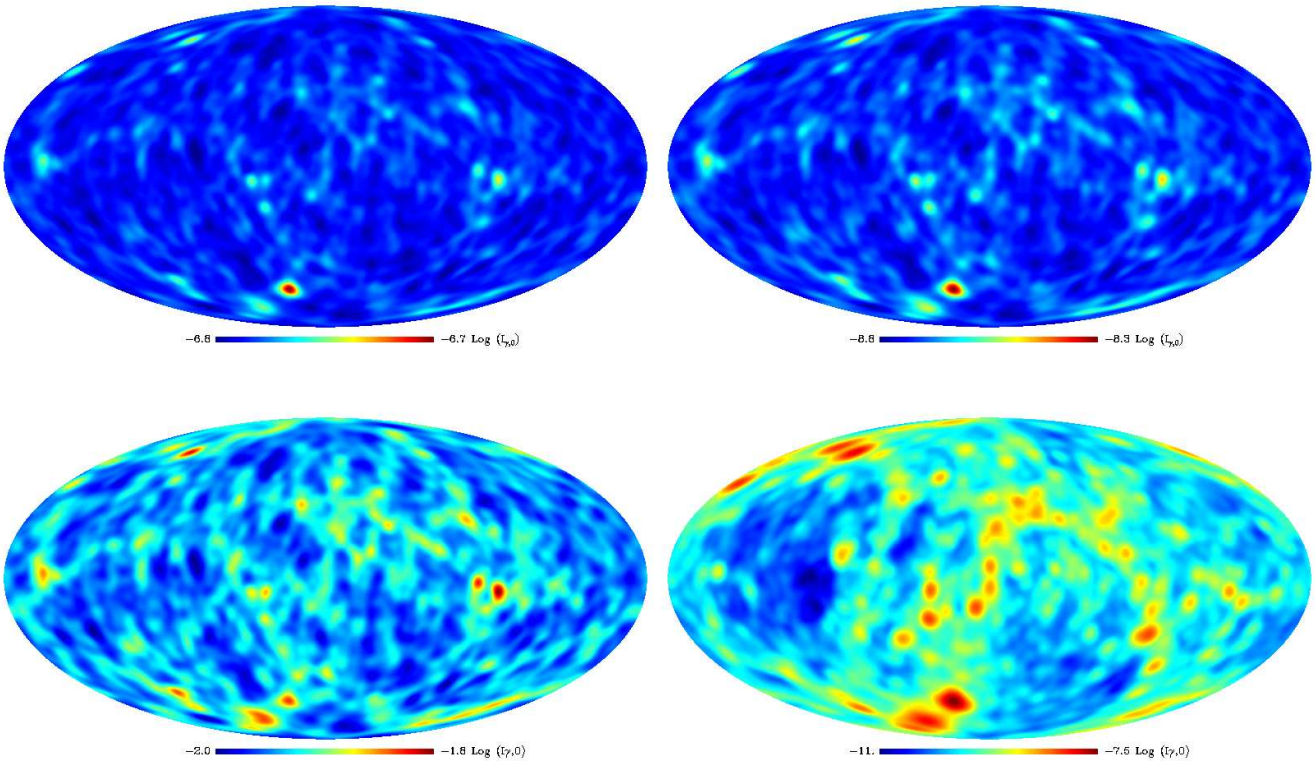

Figure 16. *Upper panel:* Total sky maps at energies $E_{\gamma,0} = 0.1\,\mathrm{GeV}$ and $E_{\gamma,0} = 32\,\mathrm{GeV}$ in the left and right, respectively. The maps were smoothed with a Gaussian beam with a FWHM of 5°. *Lower panel:* Ratio of the maps in the upper panel (left) and the partial map at $z = 0$ for $E_{\gamma,0} = 0.1\,\mathrm{GeV}$ (right).

(2009) give an approximate expression for the opacity τ following the work of Salamon & Stecker (1998): $\tau(z, E_{\gamma,0}) = z/3.3(E_{\gamma,0}/10\mathrm{GeV})^{-0.8}$. The absorption term is typically small for energies $\lesssim$ 100GeV. We carried out the exercise of producing a pair of sky maps for energies of 10 and 100 GeV including the absorption term following the parameterisation of Fornasa et al. (2009). For $E_{\gamma,0} = 10$GeV we found no significant changes compared to the map without absorption; the total value of $I_{\gamma,0}$ drops by less than 10% and the normalization of the angular power spectrum increases by $\sim 20\%$ preserving the same shape. For $E_{\gamma,0} = 100$GeV the differences are more relevant, the mean specific intensity decreases by 50%, the bump shown in the top panel of Fig. 11 (dotted line) becomes less pronounced and therefore the angular power spectrum gets closer in shape to the ones at lower energies; this is an expected effect since absorption is stronger at higher redshifts and thus reduces the contribution of the "energy bump" at this particular map.

5.7 Additional boost factor

The role and importance of annihilations of neutralinos for the EGB is subject to many uncertainties, related to both the intrinsic nature of neutralinos (as a supersymmetric particle) and to its spatial distribution (as dark matter) in the different structures in the Universe. The former uncertainties are ultimately connected to the assumed supersymmetric model, and within the mSUGRA paradigm, are approximately constrained by the results shown in Fig. 2. In our calculations, they are encapsulated in the value of the quantity f_{SUSY}. We chose a particular point, 'L', in the allowed mSUGRA parameter space as a fiducial case to obtain quantitative results. This benchmark point is close to be the upper bound for the value of f_{SUSY} and hence represents a best case scenario for a "high" value of the annihilation signal. This is important in connection with the results obtained for the expected specific intensity spectrum (Fig. 13), where the value for each energy is given by the isotropic component of our simulated sky maps. We mentioned earlier that in order to match the observational results coming from the EGRET satellite in the $1 - 10\,\mathrm{GeV}$ region, a further "boost" factor of ~ 10 appears necessary. Since the SUSY benchmark point L is close to an upper limit to the value of f_{SUSY}, this boost factor can probably not be accounted for by a different choice of parameters in the mSUGRA parameter space. Of course, the situation could be different in broader classes of SUSY theories outside the mSUGRA paradigm, but is certainly true for our analysis.

We note that there are a number effects we have not accounted for but which could possibly give such an additional boost factor: (i) We have not incorporated the effects of forming luminous galaxies onto the dark haloes; it is generally believed that the formation of a baryonic disk contracts the halo, pulling matter inwards towards the centre (e.g. Mo et al. 1998; Gnedin et al. 2004), yielding a higher concentration of the dark matter and a boost of the annihilation

flux; (ii) supermassive black holes could produce "spikes" of dark matter in the galactic centre (Gondolo & Silk 1999; Bertone & Merritt 2005). Such spikes may also yield an enhanced annihilation signal. (iii) mini-spikes of dark matter are expected to form around intermediate-mass black holes (IMBHs) (with masses in the range $10^2 \lesssim M/M_\odot \lesssim 10^6$); in certain scenarios, the gamma-ray luminosity of each mini-spike could be as large as the luminosity of the entire halo. For a typical Milky Way halo, the number of IMBHs is expected to be ~ 100 (Bertone et al. 2005); (iv) the non linear collapse of dark haloes for cold collisionless dark matter leads to the formation of caustics (e.g. Hogan 2001; White & Vogelsberger 2009), which, due to their high density can lead to a large annihilation rate and gamma-ray luminosity. However, Vogelsberger et al. (2009), using simulations of isolated haloes under self-similar and spherically symmetric initial conditions, have recently found that the contribution of caustics to the annihilation flux is less than previously expected. Based on their results, caustics are expected to produce at most a global annihilation flux comparable to the one from the smooth halo component; (v) finally, the so-called Sommerfeld enhancement, a quantum mechanical focusing effect, may lead to an effective increase of the cross section for dark matter with low velocity dispersion, such an enhancement could lead to a boost factor of several orders of magnitude (Lattanzi & Silk 2009; Bovy 2009).

6 CONCLUSIONS

Neutralinos in supersymmetric extensions of the standard model of particle physics are one of the most promising candidates for being the dominant component of dark matter in the Universe. One attractive method for their detection is to look for the products of their mutual annihilations. Among such products are γ-rays that could be produced abundantly enough in the dense centres of dark matter haloes to be susceptible of detection. In this work, we have studied the contribution of these γ-rays to the EGB radiation. Excluding the contributions from the Milky Way halo itself, all dark matter haloes and their substructures within the past light cone of an observer in our galaxy contribute to the EGB. The main goal of this paper has been to calculate the expected emission from this light-cone on the basis of the state-of-the-art Millennium-II simulation of cosmic structure formation (Boylan-Kolchin et al. 2009).

The γ-ray luminosity of each halo (or subhalo) in the simulation can be conveniently separated into two factors: (i) the SUSY factor $f_{\rm SUSY}$, encompassing the intrinsic properties of neutralinos as SUSY particles (like its mass, cross section and photon yield), and (ii) the astrophysical factor related to the density squared dependence of the annihilation rate and therefore to the clustering of neutralinos as dark matter.

We have discussed in some detail the first of these factors in Section 2, with the aim of highlighting the energy dependence of $f_{\rm SUSY}$ for a particular set of benchmark points within the mSUGRA framework. We also discussed the general mechanisms of photon production: decay of neutral pions produced during the hadronization of the primary annihilation products; (ii) loop-suppressed two-body final states containing photons; and (iii) internal bremsstrahlung (IB). Among the different benchmark points analyzed we found an uncertainty of three orders of magnitude in the normalization of $f_{\rm SUSY}$. We chose, for definiteness, one of the benchmark points with a high photon yield and a neutralino mass of $m_\chi = 185\,{\rm GeV}$ for our subsequent analysis.

We then analyzed the astrophysical factor in terms of the signals expected from main haloes and their embedded subhaloes. In order to avoid strong resolution effects, the internal structure of haloes was approximated by spherically symmetric NFW density profiles, allowing an analytic integration of the total luminosity expected from each halo. This effectively yields a scaling law where the flux from a halo can be determined by two of its structural properties alone, $V_{\rm max}$ and $r_{\rm max}$. Using this scaling law together with the abundance of haloes per unit mass range as given by the MS-II simulation, we obtained a power law description for the contribution of main haloes of a given mass interval to the total γ-ray luminosity in a cosmic volume. An extrapolation of this power law to the damping scale limit of neutralinos in the $\sim 100\,{\rm GeV}$ mass range allowed us to include the contribution of unresolved main haloes to the total gamma-ray luminosity. A similar universal power law was established for describing the contribution of subhaloes to the luminosity of their host by analyzing the most massive haloes in the MS-II containing at least 500 subhaloes. Using reasonably conservative error bounds for the large extrapolation undertaken here, we found that the "boost" factor due to substructures lies somewhere in the range 2 to ~ 1800 for a MW-size halo. With these results in mind, we note that the uncertainty in the absolute normalization of the astrophysical factor in the annihilation contribution to the EGB amounts to two to three orders of magnitude.

We implemented a new map-making procedure that for the first time allowed us to construct realistic realizations of the expected extragalactic γ-ray sky from dark matter annihilation. The angular resolution of the maps was chosen to be close to the angular resolution of the recently launched FERMI satellite, $\sim 0.115^\circ$. We found that structures up to $z \sim 2$ contribute significantly in the low to intermediate range of the energy spectrum. In particular, for an observed γ-ray energy of 10 GeV, dark matter structures beyond $z \sim 2$ contribute less than 5% to the total flux. At the highest energies, between $100 - 185\,{\rm GeV}$ for the particular benchmark point we chose, the IB contribution to the photon yield is dominant, resulting in EGB contributions that are predominantly coming from a narrow redshift range, followed by a sharp cut-off towards higher redshifts that reflects the cut-off in the energy spectrum of the $f_{\rm SUSY}$ factor.

Adopting maximum values for the expected signal boost due to substructures, we found that our prediction for the energy spectrum of the isotropic component of the EGB from dark matter annihilations lies approximately one order of magnitude below the observed values of the EGB according to the satellite EGRET, after foreground removal, in the energy range $1 - 20\,{\rm GeV}$, where an apparent excess of γ-rays has been reported. The latter has been interpreted by several authors in the past as a possible signal of dark matter annihilation. At the highest energies, IB produces a small bump in the energy spectrum that could in principle be observable but that lies orders of magnitude lower

than the expected background radiation for the particular benchmark point analyzed.

We studied the anisotropic component of the EGB by computing the angular power spectrum of the simulated maps. This yielded specific predictions for the shape of the power spectrum, which can potentially be used to discriminate against other sources of γ-rays, since the annihilation signal depends in a specific and unique way on the large scale distribution of haloes, on the distribution of subhaloes within haloes, and on the abundance and internal structure of haloes as a function of time. The shape of the power spectrum was found to depend on the energy of the observations. Interestingly, these differences can be exploited to construct 'color' maps that enhance the signal of nearby dark matter structures, akin to hardness ratio maps in X-ray observations. For example, we found that taking the ratio of the maps at energies of 0.1 GeV and 32 GeV greatly enhances the contrast of local dark matter structures, making them clearly visible in the γ-ray sky. If strong spectral features in the rest-frame emission spectrum of the annihilation radiation are present, this could be especially powerful, perhaps even allowing tomographic observations of dark matter structures.

Although the subtraction of foreground radiation and other astrophysical sources contributing to the EGB is a difficult task, the specific shape of the contribution of dark matter annihilation to the power spectrum of the EGB makes this statistical tool attractive for potentially detecting dark matter in the near future (as has been pointed out previously by, e.g., Ando & Komatsu 2006). The maps we constructed in this work are a particular useful tool to help designing and testing data analysis methods for uncovering this signal from real data. Also, we have here been able to show that the energy dependence of the signal offers an additional highly attractive way to detect specific signatures of the annihilation emission spectrum. It is quite possible that the different energy channels onboard the satellite FERMI that is currently mapping the EGB will already allow a fruitful application of such an approach.

ACKNOWLEDGMENTS

JZ would like to thank Simon D. M. White, Mark Vogelsberger and Darío Núñez for interesting and critical discussions. JZ is supported by the Joint Postdoctoral Program in Astrophysical Cosmology of the Max Planck Institute for Astrophysics and the Shanghai Astronomical Observatory. Some of the results in this paper have been derived using the HEALPiX (Górski et al. 2005) package.

REFERENCES

Abdo A. A., Ackermann M., Ajello M., et al., 2009, Phys. Rev. Lett., 102, 181101
Adriani O., Barbarino G. C., Bazilevskaya G. A., et al., 2009, Nature, 458, 607
Akerib D. S., Alvaro-Dean J., Armel-Funkhouser M. S., et al., 2004, Phys. Rev. Lett., 93, 211301
Alner G. J., Araujo H., Arnison G. J., et al., 2005, Astropart. Physics, 23, 444
Ando S., 2009, Phys. Rev. D, 80, 023520
Ando S., Komatsu E., 2006, Phys. Rev. D, 73, 023521
Ando S., Komatsu E., Narumoto T., Totani T., 2007a, MNRAS, 376, 1635
Ando S., Komatsu E., Narumoto T., Totani T., 2007b, Phys. Rev. D, 75, 063519
Angle J., Aprile E., Arneodo F., et al., 2008, Phys. Rev. Lett., 100, 021303
Atwood W. B., Abdo A. A., Ackermann M., et al., 2009, ApJ, 697, 1071
Baer H., Balázs C., 2003, J. Cosmol. Astropart. Phys., 5, 6
Baer H., Paige F. E., Protopescu S. D., Tata X., 2003, preprint (hep-ph/0312045)
Baltz E. A., Edsjö J., 1999, Phys. Rev. D, 59, 023511
Battaglia M., Roeck A. D., Ellis J., Gianotti F., Olive K. A., Pape L., 2004, European Phys. J. C, 33, 273
Bélanger G., Kraml S., Pukhov A., 2005, Phys. Rev. D, 72, 015003
Belikov A. V., Hooper D., 2009, preprint (arXiv:0906.2251)
Berezinsky V., Bottino A., Ellis J., Fornengo N., Mignola G., Scopel S., 1996, Astropart. Phys., 5, 333
Berezinsky V., Dokuchaev V., Eroshenko Y., 2003, Phys. Rev. D, 68, 103003
Bergström L., Bringmann T., Edsjö J., 2008, Phys. Rev. D, 78, 103520
Bergström L., Edsjö J., Zaharijas G., 2009, Phys. Rev. Lett., 103, 031103
Bernabei R., Belli P., Cappella F., et al., 2008, European Phys. J. C, pp 167–+
Bernabei R., Belli P., Cerulli R., et al., 2000, Phys. Lett. B, 480, 23
Bertone G., 2007, preprint (0710.5603)
Bertone G., Merritt D., 2005, Phys. Rev. D, 72, 103502
Bertone G., Zentner A. R., Silk J., 2005, Phys. Rev. D, 72, 103517
Bovy J., 2009, Phys. Rev. D, 79, 083539
Boylan-Kolchin M., Springel V., White S. D. M., Jenkins A., Lemson G., 2009, MNRAS, 398, 1150
Bringmann T., 2009, New J. Phys., 11, 105027
Bringmann T., Bergström L., Edsjö J., 2008, J. High Energy Phys., 1, 49
Bullock J. S., Kolatt T. S., Sigad Y., Somerville R. S., Kravtsov A. V., Klypin A. A., Primack J. R., Dekel A., 2001, MNRAS, 321, 559
Carbone C., Springel V., Baccigalupi C., Bartelmann M., Matarrese S., 2008, MNRAS, 388, 1618
Chang J., Adams J. H., Ahn H. S., et al., 2008, Nature, 456, 362
Cuoco A., Brandbyge J., Hannestad S., Haugbølle T., Miele G., 2008, Phys. Rev. D, 77, 123518
Cuoco A., Hannestad S., Haugbølle T., Miele G., Serpico P. D., Tu H., 2007, J. Cosmol. Astropar. Phys., 4, 13
de Boer W., 2008, in Hong P. K. . D. K., ed., American Institute of Physics Conference Series Vol. 1078, Indirect Dark Matter Signals. pp 108–115
de Boer W., Herold M., Sander C., Zhukov V., Gladyshev A. V., Kazakov D. I., 2004, preprint (astro-ph/0408272)
de Boer W., Nordt A., Sander C., Zhukov V., 2007, A&A, 470, 61
Dermer C. D., 2007, in S. Ritz P. Michelson . C. A. M., ed., The First GLAST Symposium Vol. 921, The Extragalactic γ Ray Background. pp 122–126

Diemand J., Kuhlen M., Madau P., Zemp M., Moore B., Potter D., Stadel J., 2008, Nature, 454, 735
Diemand J., Moore B., Stadel J., Kazantzidis S., 2004, MNRAS, 348, 977
Eke V. R., Navarro J. F., Steinmetz M., 2001, ApJ, 554, 114
Elsässer D., Mannheim K., 2005, Phys. Rev. Lett., 94, 171302
Falvard A., Giraud E., Jacholkowska A., et al., 2004, Astropart. Phys., 20, 467
Feng J. L., 2005, Ann. Phys., 315, 2
Fornasa M., Pieri L., Bertone G., Branchini E., 2009, Phys. Rev. D, 80, 023518
Fornengo N., Pieri L., Scopel S., 2004, Phys. Rev. D, 70, 103529
Freese K., Gondolo P., Stodolsky L., 2001, Phys. Rev. D, 64, 123502
Gao L., Navarro J. F., Cole S., Frenk C. S., White S. D. M., Springel V., Jenkins A., Neto A. F., 2008, MNRAS, 387, 536
Gnedin O. Y., Kravtsov A. V., Klypin A. A., Nagai D., 2004, ApJ, 616, 16
Gondolo P., Edsjö J., Ullio P., Bergström L., Schelke M., Baltz E. A., 2004, J. Cosmol. Astropart. Phys., 7, 8
Gondolo P., Edsjö J., Ullio P., Bergstrom L., Schelke M., Baltz E. A., 2005, New Astronomy Rev., 49, 149
Gondolo P., Gelmini G., 1991, Nuclear Phys. B, 360, 145
Gondolo P., Silk J., 1999, Phys. Rev. Lett., 83, 1719
Górski K. M., Hivon E., Banday A. J., Wandelt B. D., Hansen F. K., Reinecke M., Bartelmann M., 2005, ApJ, 622, 759
Green A. M., Hofmann S., Schwarz D. J., 2004, MNRAS, 353, L23
Heister A., Schael S., Barate R., et al., 2004, Phys. Lett. B, 583, 247
Hofmann S., Schwarz D. J., Stöcker H., 2001, Phys. Rev. D, 64, 083507
Hogan C. J., 2001, Phys. Rev. D, 64, 063515
Hooper D., 2007, preprint (0710.2062)
Jacholkowska A., Lamanna G., Nuss E., et al., 2006, Phys. Rev. D, 74, 023518
Jeltema T. E., Kehayias J., Profumo S., 2009, Phys. Rev. D, 80, 023005
Jubelgas M., Springel V., Enßlin T., Pfrommer C., 2008, A&A, 481, 33
Kneiske T. M., 2008, Chinese J. Astronomy and Astrophysics Suppl., 8, 219
Kneiske T. M., Mannheim K., 2008, A&A, 479, 41
Komatsu E., Dunkley J., Nolta M. R., et al., 2009, ApJS, 180, 330
Lattanzi M., Silk J., 2009, Phys. Rev. D, 79, 083523
Lavalle J., Manseri H., Jacholkowska A., et al., 2006, A&A, 450, 1
Loeb A., Zaldarriaga M., 2005, Phys. Rev. D, 71, 103520
Lundberg J., Edsjö J., 2004, Phys. Rev. D, 69, 123505
Martin S. P., 1998, in Kane G. L., ed., Perspectives on Supersymmetry, A Supersymmetry Primer. pp 1–+
Miniati F., 2002, MNRAS, 337, 199
Miniati F., Koushiappas S. M., Di Matteo T., 2007, ApJ, 667, L1
Mo H. J., Mao S., White S. D. M., 1998, MNRAS, 295, 319
Mo H. J., White S. D. M., 1996, MNRAS, 282, 347
Nath P., 2003, preprint (hep-ph/0307123)
Navarro J. F., Frenk C. S., White S. D. M., 1997, ApJ, 490, 493
Navarro J. F., Ludlow A., Springel V., et al., 2009, MNRAS, pp 1918–+
Neto A. F., Gao L., Bett P., et al., 2007, MNRAS, 381, 1450
Nilles H. P., 1984, Phys. Rep., 110, 1
Núñez D., Zavala J., Nellen L., Sussman R. A., Cabral-Rosetti L. G., Mondragón M., 2008, J. Cosmol. Astropart. Phys., 5, 3
Ong R. A., 2006, preprint (astro-ph/0605191)
Profumo S., Jeltema T. E., 2009, J. Cosmol. and Astropart. Phys., 7, 20
Salamon M. H., Stecker F. W., 1998, ApJ, 493, 547
Sheth R. K., Mo H. J., Tormen G., 2001, MNRAS, 323, 1
Siegal-Gaskins J. M., 2008, J. Cosmol. Astropart. Phys., 10, 40
Siegal-Gaskins J. M., Pavlidou V., 2009, Phys. Rev. Lett., 102, 241301
Spooner N. J. C., 2007, J. Phys. Society of Japan, 76, 111016
Springel V., 2005, MNRAS, 364, 1105
Springel V., Frenk C. S., White S. D. M., 2006, Nature, 440, 1137
Springel V., Wang J., Vogelsberger M., et al., 2008, MNRAS, 391, 1685
Springel V., White S. D. M., Frenk C. S., et al., 2008, Nature, 456, 73
Springel V., White S. D. M., Tormen G., Kauffmann G., 2001, MNRAS, 328, 726
Stadel J., Potter D., Moore B., Diemand J., Madau P., Zemp M., Kuhlen M., Quilis V., 2009, MNRAS, 398, L21
Steffen F. D., 2006, J. Cosmol. and Astropart. Phys., 9, 1
Steffen F. D., 2007, preprint (arXiv:0711.1240)
Stoehr F., White S. D. M., Springel V., Tormen G., Yoshida N., 2003, MNRAS, 345, 1313
Strigari L. E., Beacom J. F., Walker T. P., Zhang P., 2005, J. Cosmol. Astropart. Phys., 4, 17
Strong A. W., Moskalenko I. V., Reimer O., 2004, ApJ, 613, 956
Taylor J. E., Silk J., 2003, MNRAS, 339, 505
Torii S., Yamagami T., Tamura T., et al., 2008, preprint (arXiv:0809.0760)
Ullio P., Bergström L., Edsjö J., Lacey C., 2002, Phys. Rev. D, 66, 123502
Vogelsberger M., Helmi A., Springel V., et al., 2009, MNRAS, 395, 797
Vogelsberger M., White S. D. M., Helmi A., Springel V., 2008, MNRAS, 385, 236
Vogelsberger M., White S. D. M., Mohayaee R., Springel V., 2009, MNRAS, 400, 2174
White S. D. M., Vogelsberger M., 2009, MNRAS, 392, 281
Wood M., Blaylock G., Bradbury S. M., et al., 2008, ApJ, 678, 594
Zhao D. H., Jing Y. P., Mo H. J., Börner G., 2003, ApJ, 597, L9